Building a three dimensional model of the active Plio-Quaternary basin of Argostoli (Cephalonia Island, Greece): an integrated geophysical and geological approach

Edward Marc Cushing, Fabrice Hollender, Denis Moiriat, Cédric Guyonnet-Benaize, Nikolaos Theodoulidis, Sophie Sepulcre, Edwige Pons-Branchu, Pierre-Yves Bard, Cécile Cornou, Aline Dechamp, et al.

To cite this version:

Edward Marc Cushing, Fabrice Hollender, Denis Moiriat, Cédric Guyonnet-Benaize, Nikolaos Theodoulidis, et al.. Building a three dimensional model of the active Plio-Quaternary basin of Argostoli (Cephalonia Island, Greece): an integrated geophysical and geological approach. Engineering Geology, 2020, 265, pp.105441. 10.1016/j.enggeo.2019.105441 . hal-02404456

HAL Id: hal-02404456
https://hal.science/hal-02404456v1

Submitted on 8 Jul 2020

Engineering Geology 265 (2020) 105441

Contents lists available at ScienceDirect

Engineering Geology

journal homepage: www.elsevier.com/locate/enggeo

Building a three dimensional model of the active Plio-Quaternary basin of Argostoli (Cephalonia Island, Greece): An integrated geophysical and geological approach

Edward Marc Cushing[a,*], Fabrice Hollender[b,c], Denis Moiriat[a], Cédric Guyonnet-Benaize[b], Nikolaos Theodoulidis[d], Edwige Pons-Branchu[e], Sophie Sépulcre[f], Pierre-Yves Bard[c], Cécile Cornou[c], Aline Dechamp[g], Armand Mariscal[c,i], Zafeiria Roumelioti[h]

[a] IRSN, Fontenay-aux-Roses, France
[b] CEA, DEN, Saint-Paul-les-Durance, France
[c] ISTerre, Université Grenoble-Alpes, CNRS, IRD, IFSTTAR, Grenoble, France
[d] ITSAK, Thessaloniki, Greece
[e] LSCE/IPSL, CEA-CNRS-UVSQ, Université Paris-Saclay, France
[f] GEOPS, Université Paris-Saclay, France
[g] CEA, DIF, Bruyères le Chatel, France
[h] Aristotle University, Thessaloniki, Greece
[i] IGE, Université Grenoble, CNRS, IRD, Grenoble, France.

ARTICLE INFO

Keywords:
3D Geological modeling
Surface waves techniques
Sedimentary basin
Cephalonia - Greece - Site effects

ABSTRACT

This work is a multidisciplinary approach from geological and geophysical surveys to build a 3D geological model of Argostoli Basin (Cephalonia Island, Greece) aiming to be used for computational 3D simulation of seismic motion. Cephalonia Island is located at the north-western end of the Aegean subduction frontal thrust that is linked to the dextral Cephalonia Transform Fault (west of Cephalonia) where the seismic hazard is high in terms of earthquake frequency and magnitude. The Plio-Quaternary Koutavos-Argostoli basin site was selected within the French Research Agency PIA SINAPS@ project (www.institut-seism.fr/projets/sinaps/ - last accessed on November 25th 2019) to host a vertical accelerometer array. The long-term goal is to validate three-dimensional nonlinear numerical simulation codes to assess the site-specific amplification and nonlinearity. Herein the geological and geophysical surveys carried out from 2011 to 2017 are presented and in particular the complementary investigations that led to the identification of the main stratigraphic units and their structures. In addition, coral debris sampled from the vertical array deep borehole cores were used for $^{230}Th/^{234}U$ measurements, which confirmed the Pleistocene age of the Koutavos basin. The characterization of the three-dimensional structure of the stratigraphic units was achieved by coupling geological cross-sections (i.e., depth geometry) and geophysical surveys based of surface wave analysis.

1. Introduction

The sedimentary basin of Argostoli (Fig. 1) of Cephalonia Island in western Greece represents a site of special scientific interest for studying site effects and the nonlinear behavior of soil during an earthquake considering its geological structure and the high seismicity rate. This island was particularly affected by an $M_W = 7.3$ earthquake in 1953 that caused a seismic uplift of its southern par up to one meter. In 2014, a sequence of earthquakes caused very high PGA (maximum ever recorded in Greece, in Lixouri town up to 0.77 g). The Argostoli basin comprises lagoonal Quaternary sediments that overlies the infilling of an active Plio-Quaternary syncline. The active tectonics is highlighted by intense folding and faulting of the Plio-Quaternary series on the peninsula west of Argostoli and its extension toward the south-east.

This basin has been studied since the 1990's with the installation of a first vertical accelerometer network (Ionianet) by the National Technical University of Athens (Protopapa et al., 1998). In 2011–2012, a set of seismic measurements were carried out in the framework of experiments of the Network of European Research Infrastructures for

---

* Corresponding author.
E-mail address: edward.cushing@irsn.fr (E.M. Cushing).

https://doi.org/10.1016/j.enggeo.2019.105441
Received 24 July 2019; Received in revised form 28 November 2019; Accepted 29 November 2019

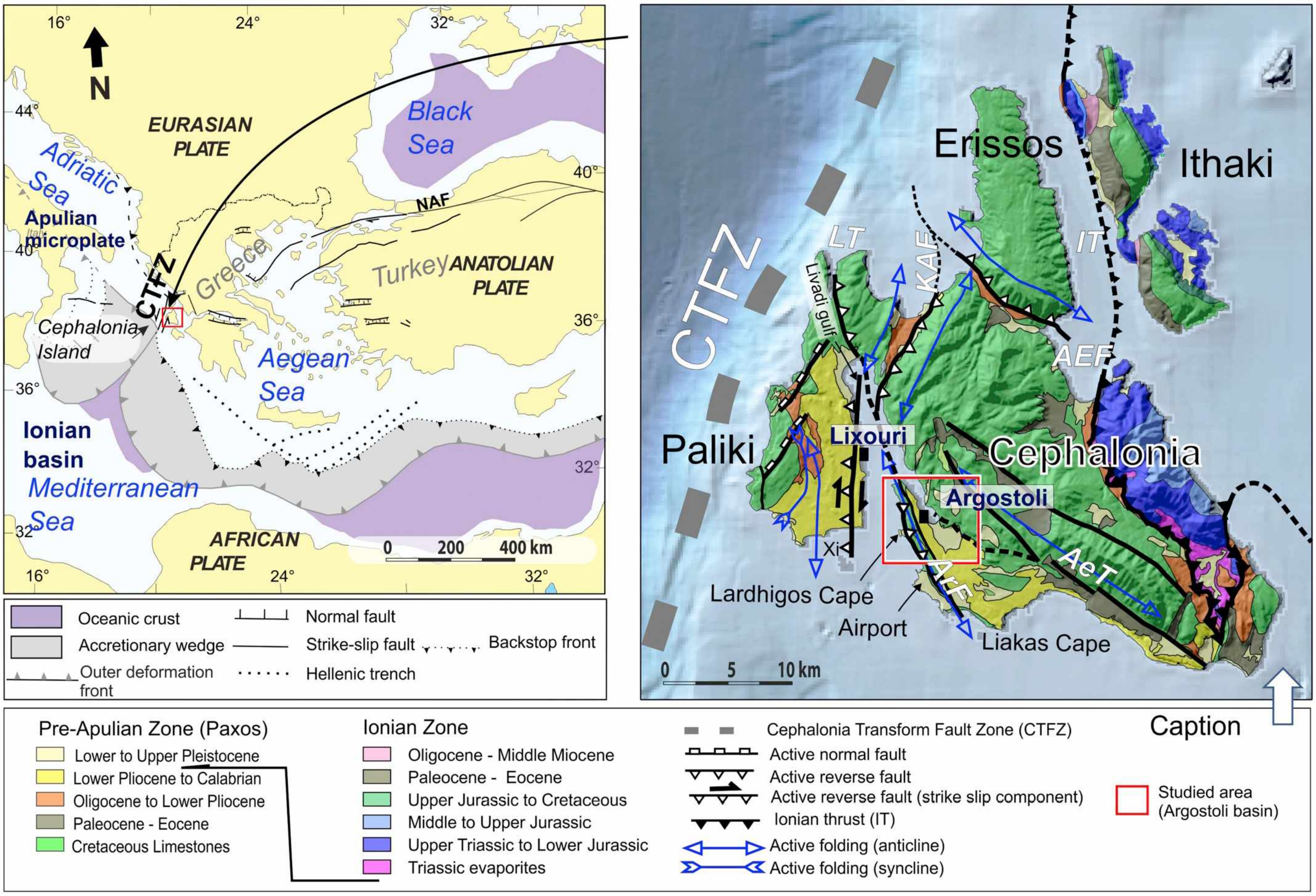

Fig. 1. Left: Geodynamic map of the broader southeastern Mediterranean. Right: Geology and and prevailing seismotectonic features of the Cephalonia and Ithaca Islands (synthesis based on maps of Sorel (1989), Underhill (1989), Stiros et al. (1994), Lagios et al., 2012, Lekkas (1996), also from the 2014 post seismic geodetic data (Boncori et al., 2015; Ganas et al., 2015) and of data from our geological survey). IT, Ionian Thrust (thrust over lower Pliocene or older series of the Pre-Apulian zone – black arrow in the key); KAF, Kontogourata-Agon Fault; ArF, Argostoli fault (encompassing at this scale same parallel tending faults: White Rock and Minies faults - not drawn); LT, Livadi Thrust; CTFZ, Cephalonia Transform Fault Zone. Map modified from Theodoulidis et al., (2018a).

Earthquake Risk Assessment and Mitigation (NERA project FP7 n° 262,330). In 2013, based on initial observation, a first survey was conducted to collect geological and geophysical data in the framework of the ANR PIA SINAPS@ project of the French Research Agency (ANR) (Berge-Thierry et al., 2017, Berge-Thierry et al., 2019, Theodoulidis et al., 2018b, https://www.institut-seism.fr/en/projects/sinaps/). At the beginning of 2014, a seismic sequence including two events of magnitude of about $M_W = 6$ was observed (Theodoulidis et al., 2016) and a 'post-seismic' campaign for additional measurements followed closely (Perron et al., 2018). After June 2015, four boreholes were drilled in the Koutavos area, and several accelerometers were installed on surface as well as at different depths establishing the vertical array ARGONET (ARGOstoli NETwork; http://argonet-kefalonia.org) and producing high quality datasets (Theodoulidis et al., 2018a). All these records already led to several works focused on rotation wavefield analysis (Sbaa et al., 2017) or spatial coherency analysis (Svay et al., 2017; Imtiaz et al., 2018), among others.

In order to construct a geological model aiming to perform numerical simulation to study site effects, a fine geological characterization of this basin was necessary. The geometries of different geological units have remained poorly detailed at the basin scale yet. In this way, this work presents the results of characterization of this basin based on geological and geophysical surveys carried out from 2011 to 2017. The geological surveys are based on geological mapping the new boreholes in the Koutavos. The geophysical surveys are based on vibration measurements for horizontal-to-vertical spectral ratio (HVSR) analysis as well surface-wave dispersion analysis (SWDA). All these results lead to draw of a revised geological map of the Argostoli basin and to build the 3D basin structure which could be used in the future numerical analysis.

First we present the geodynamical context of the research area, and then we present the previous geological and structural knowledge of the Argostoli basin. Next, we detail new geological information gathered from both reconnaissance and boreholes surveys and new dating information. The third part is devoted to the description and the analysis of the results of the geophysical surveys based on SWDA and HVSR techniques. We finally present the used methodology to build a 3 dimensional model from the combination and cross-check of the previous geological and geophysical information.

1.1. Geodynamics framework

Western Greece is one of the main active tectonics areas of the Mediterranean region, with the highest seismic activity in Europe. Cephalonia Island is located in the western part of the fold-and-thrust belt of the Hellenic Foreland (Fig. 1) (Hatzfeld et al., 1989; Sorel, 1989; Underhill, 1989). In this region, the lithology is mainly Alpine Triassic, Mesozoic, and Cenozoic sedimentary deposits (e.g., Aubouin, 1959; Aubouin and Dercourt, 1962). The Cephalonia area is located at the boundary of the Eurasian/ African plates, which is characterized by a convergence rate of up to 35 mm/yr (e.g., Reilinger et al., 2006). In this area, this convergence arises from the northwestern end of the Aegean subduction frontal thrust, which is almost flat and is located at about 10 to 12 km in depth under the Pre-Apulian continental basement (Clément et al., 2000; Sachpazi et al., 2000). This basement pushes on the accretionary prism of the Mediterranean ridge (Nielsen Dit Christensen, 2003). The frontal thrust outcrops at the southwestern edge of the Mediterranean ridge, > 200 km south of Zante (Zakinthos) Island. To the north, the Aegean Arc terminates at the dextral Cephalonia Transform Fault (CTF), which is located along the west coast of Lefkas (Lefkada) and Cephalonia Islands (e.g., Cushing, 1985; Scordilis et al., 1985), with a dextral slip that was estimated at 17 mm/yr by Pérouse (2013). This major strike-slip fault has the role of a transition zone between the African subducting plate and the continental Apulian microplate (Le Pichon et al., 1995; Louvari et al., 1999; Sachpazi et al., 2000; Nielsen Dit Christensen, 2003; Pérouse, 2013; Pérouse et al., 2017).

Due to the dimensions of the CTF and the other overriding thrusts (Stiros et al., 1994; Basili et al., 2013; DISS Working Group, 2015) linked to the Aegean subduction and to the high convergence rate, the seismic hazard is high in terms of earthquake re-occurrence and magnitude. This is why major earthquakes can and have occurred with the most destructive recent one being the 1953, $M_W = 7.2$ earthquake. The co-seismic movement associated with this event provoked an uplift of about 0.5 to 1.0 m of a large part of Cephalonia Island (Stiros et al., 1994). Another paleoseismic event previously uplifted the southern part of the island by about 0.6 m, as deduced from an analysis of the uplifted notches (Stiros et al., 1994). > 20 earthquakes with magnitudes from 6.0 to 7.2 have caused damage in the surrounding areas since the 17th century (Papathanassiou et al., 2017; Theodoulidis et al., 2016). The more recent earthquakes (i.e., since 1983) have mainly been located on the CTF or on secondary associated faults, such as those of: January 17, 1983 ($M_W = 7.2$), on the southern segment of the CTF; August 14, 2003 ($M_W = 6.2$) in Lefkas; January 26, 2014 ($M_W = 6.1$) and February 3, 2014 ($M_W = 6.0$) in Lixouri (e.g. Papathanassiou et al., 2016); and November 17, 2015 ($M_W = 6.4$) in Lefkas. Seismic and geodetic monitoring and InSAR imagery have contributed to the more accurate delineation of the faults (Boncori et al., 2015; Briole et al., 2015; Avallone et al., 2017; Saltogianni et al., 2018). In particular, a N-S trending strike slip fault is inferred from the analysis of geodetic data gathered after the 2014 earthquakes in Cephalonia (Boncori et al., 2015; Ganas et al., 2015), see Fig. 1. Complementary information regarding structural data (e.g., the presence of normal faults in western Paliki) was provided by Nielsen Dit Christensen (2003), Pérouse (2013) and Hunter (2013). These faults represent an en-echelon belt that is aligned against the CTF from Lefkas to the southernmost banks offshore of the Paliki peninsula (Fig. 1). This framework can be interpreted as a bulging extension along the transcurrent and compressive major faults. Moreover, marine seismic reflection profiles performed in the Livadi Gulf and to the south of Paliki underline the intense deformation to the east of the Lixouri shoreline (i.e., both N-S folding and normal faults) (Hunter, 2013).

1.2. State of knowledge about the Geology of the Argostoli area

The regional geology of the Cephalonia Island have extensively been studied and mapped (e.g. British Petroleum Co., 1971; Sorel, 1976; Institute of Geology and Mineral Exploration IGME, 1985; Sorel, 1989; Underhill, 1989; Stiros et al., 1994; Lekkas, 1996; Hunter, 2013). In the Argostoli cape area, the authors have particularly pointed out the importance of the Plio-Quaternary deformation (folds, faulting and uplifted markers such as marine terraces) of the western part of the Argostoli area (Argostoli peninsula) including both the Argostoli basin and Minies anticline.

The series of the Argostoli-Minies anticline (relief that constitutes the Argostoli peninsula) and the Argostoli syncline (depression located in the gulf of Argostoli and southward in the Koutavos lagoon and the Kokolata plain) can be described as presented in Fig. 2 where the indicated nomenclature will be used afterward in this paper: i.e., Cretaceous, *C*; Eocene, *E*; Miocene to Lower Pliocene, *M-P*, Pliocene, *P*[*a, b*]; Pleistocene, *Pt*-[*a, b, c, d, s, m, k*]; and Holocene, *H*:

At the bottom of the series, the entire outcropping Cretaceous unit (C) for Cephalonia has been estimated to be approximately 1700 m thick (British Petroleum Co. Ltd, 1971; Sorel, 1976, 1989) and characterized by a Lower Cretaceous (Barremian to Albian) unit defined by well-bedded and yellowish dolomitic limestone, and an Aptian to Maastrichtian Cretaceous unit made of biodetritic to sub-recifal limestone with rudists. Locally, near White Rock Faults, this limestone is strongly tectonically brecciated (Sorel, 1989; Underhill, 1989). In the Minies anticline area, there are Eocene- to Paleocene-bedded porcellaineous limestone outcrops (E, in Fig. 2).

Above the Cretaceous and Paleocene-Eocene limestone, there are local outcrops of a conformable series of Miocene to lower Pliocene detritic series such as, calcareous marls, gray clays, and blue marls in narrow synclines that can be dated for the more recent formation by the presence of *G. margaritae* planktonic foraminifera (observed at Liakas Cape and Lixouri). A first unconformity is determined in western Cephalonia by the presence of *Globorotalia puncticulata* in unconformable clayey grainstones over sandy clay encompassing *G. margaritae* planktonic foraminifera (observed at Liakkas Cape and Lixouri - Sorel, 1989). This first deformation episode occurred in the lower Pliocene (between 4 and 3 Ma – Sorel et al., 1992).

From the end of lower Pliocene (~4 Ma) to Calabrian, the series correspond to unconformable breccias and calcareous sandstone described by Underhill (1989) as a delta fan sequence (*Pa*), which is followed by thick blue marl formations (*Pb*) and ends with sandy marls and gravel (*Pt-a*) then Calabrian calcareous sandstone delta fans (*Pt-b*). In the Argostoli cape area, this sequence is strongly folded and faulted by a second episode of deformation that is estimated to be post Calabrian and precede middle Pleistocene continental breccias slopes and is proposed by Sorel et al. (1992) to occur during a period between 1.0 and 0.7 Ma. The middle Pleistocene unit is represented by strongly cemented slope breccias (*Pt-c*) previously called 'Mindelian' (Sorel, 1989; Underhill, 1989). These breccias are overlaid by screes (*Pt-s*) (previously called 'Rissian') that are laterally connected to the uplifted terrace constituted by beach rock (*Pt-m*) previoulsly called 'Paleo-Milazian'). These raised beaches are uplifted up to 100 m above sea level in the southern part of the investigated area north of the Minies Village (Sorel,1989). These Upper Pleistocene to Present (*Pt-d*) cover (few meters) lies over the isthmus of the Lardhigos cape (Fig. 2);

In the Argostoli-Koutavos area, the Plio-Pleistocene series is not detailed by authors and is always divided in two units (generally Plio-Pleistocene and more recent): Mio-Pliocene blue-gray marls series and alluvium is mapped by BP (1971), lower Pliocene to Pleistocene series have been mapped (BP co., 1971), Pliocene and Holocene (IGME, 1985), Plio-Pleistocene and Riss to present (Underhill, 1989), Plio-Calabrian clastic formation and recent alluvium and interglacial Middle Pleistocene deposits (Lekkas, 1996). The more recent unit in the Argostoli basin is the Holocene and artificial deposits (i.e., ~2 m of man-made infill - (Hadler, 2013)) in the Koutavos Park area. They include a succession of thin distinct tsunamigenic layers with ages that have been determined by radiocarbon dating to about 6000 BP for the oldest event (Hadler, 2013) at about 7 m below present sea level (b.s.l.).

On the structural point of view, the axis of the Argostoli sedimentary basin strikes NW-SE. It is located on the eastern flank of the west-verging Argostoli-Minies anticline (Fig. 1). The Argostoli-Minies anticline is faulted at least by two main east-dipping reverse faults: the White Rock Fault and the Argostoli Fault (Underhill, 1989) (Fig. 2). It is not clear if the Minies Fault described by Sorel (1989) corresponds to the White rock fault or is another structure. The deformation associated with these faults is locally intense, with brecciated and dolomitized limestone. On the footwall of the White Rock fault several minor reverse bedding plane slip faults with western dip cut the Pleistocene screes (*Pt-s*) and terrace (*Pt-m*) (Sorel, 1976, 1989) were identified near

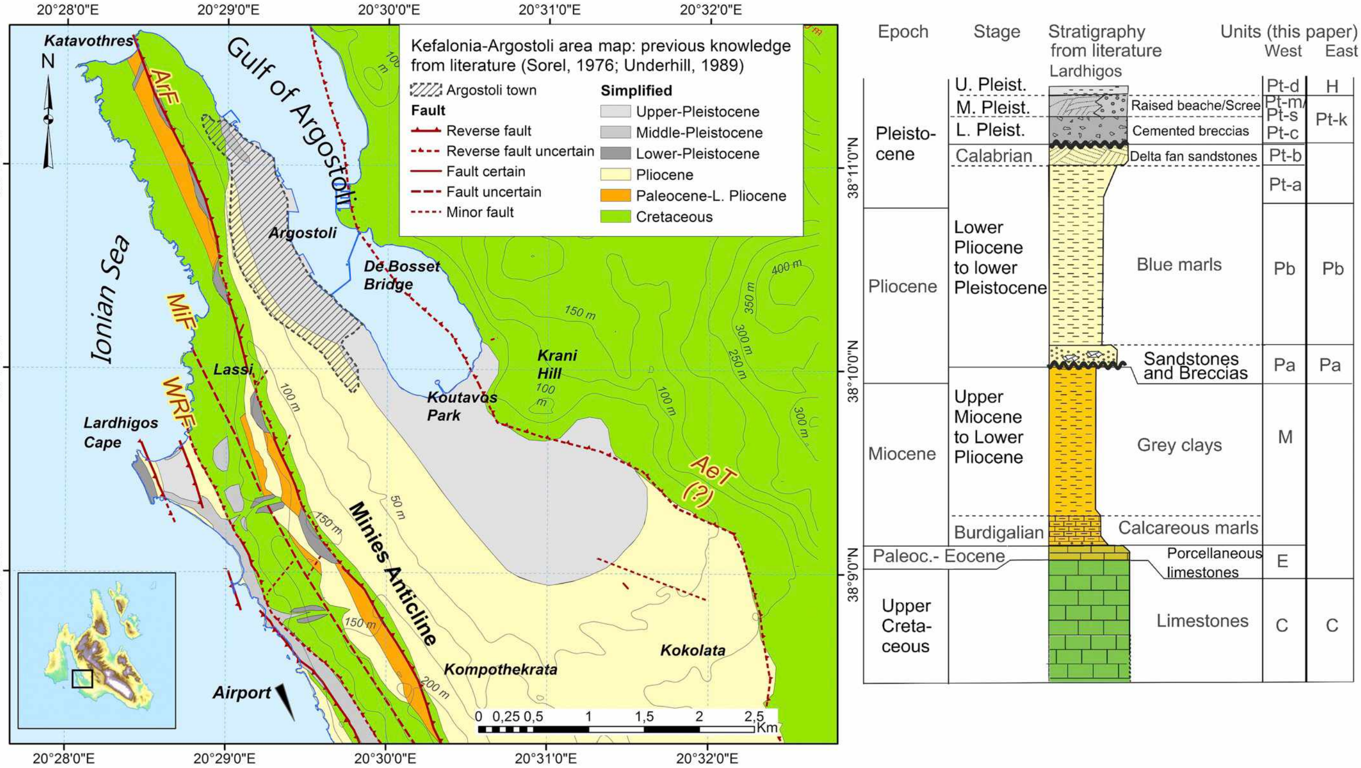

Fig. 2. Geological map from previous works (mainly from Sorel, 1976, 1989; Underhill, 1989). Detailed information about the Plio-Pleistocene series of the Argostoli basin was not then available. A Lithostratigraphic log (not to scale) of the Argostoli-Minies Anticline is presented at the right. This log is constructed from the geological description provided by the above mentioned authors. The correspondence with the nomenclature used in this article is reported on the right column. The 'West' column describes the units that have been defined for the Argostoli-Minies anticline while the 'East' column displays the units that can be observed in the Argostoli-Koutavos basin.

the Lardhigos cape and more to the south up to the Airport area.

We remark that on the eastern side of the Argostoli basin, (Underhill, 1989) proposed that the Aenos thrust (*AeT* see in Figs. 1, 2) lies at the base of the hillslopes at the foothills of Aenos Mountain and has been active after the late Piacienzian by Underhill. This local topography was, however, not interpreted as having a tectonic origin, but as the result of paleo-cliffs along the shore of the Pliocene Sea (Sorel, 1976; Sorel et al., 1992).

2. New information based on geological surveys

2.1. Geological mapping

2.1.1. Complementary stratigraphy of the Argostoli basin

One notes that the previous geological studies have not distinguished any subdivision in the lower Pliocene to lower-middle Pleistocene series of the Argostoli basin (i.e. east of Minies Anticline). During this geological survey of the area, we identified 3 main units that could be linked with the described units in the western flank of the Argostoli-Minies anticline. This new subdivision in the lower Pliocene to lower-middle Pleistocene series constitutes the main change regarding previous geological mappings. The description below concerns the series that outcrops in the Argostoli-Koutavos basin:

- The basal unit is coarse, much consolidated (calcareous breccias), and has a dip of about 30° to the ENE. On the slope located south of the town of Argostoli, three hectometric ledges reveal the presence of softer sediments (clayey sands) interbedded in the harder sandstone levels that could correspond to an alternation of coarse and thinner sediments in the delta fan series. We link this unit with the ***Pa* unit** of the western flank of the anticlinal. On this eastern flank, the basal contact of the *Pa* unit with the Cretaceous limestones is an erosional and angular unconformity. Toward the east, this unit doesn't outcrop in the center of the Argostoli basin and this thickness is likely reduced in this direction which was confirmed by the geophysical surveys (see paragraph 3);
- Lying over this first unit, a series of alternations of sands and sandstone dipping toward the East along the eastern Argostoli anticlinal flank (well exposed in some southern quarters of the town of Argostoli). Toward the south, this unit is more flat and coarser with gravel and breccias indicating lithological variation as described by Sorel (1989). We correlate this unit with the Piacenzian clay series belonging to west flank of the Minies anticline (***Pb* unit**); The geological mapping allows to assert that the thickness of Unit *Pb*like the *Pa*unit decreases toward the East until it disappears under the upper series (*Pt-k*) identified hereafter;
- The Quaternary unit described by Sorel and Underhill (1989) as 'Wurmian to present deposits' outcrops in the center of the Argostoli basin and forms lowlands around the Koutavos area. Some outcrops such as clay quarry, west of Koutavos Park, show yellowish to reddish sandy clays. This unit is defined as the ***Pt-k* unit** (Pleistocene of Koutavos Park);

In addition of the Plio-Pleistocene to proposed stratigraphy, we distinguished the Holocene deposits that are located only in the vicinity of the Koutavos Park. This ***H* unit** is composed of lagoonal sediments overlain by backfill (Hadler, 2013; Theodoulidis et al., 2018a).

2.1.2. Complementary structural information

During our field survey, we completed dip measurements and outcrop observations. We mostly confirmed the structural framework of the western part of the Minies anticline. We kept the Minies fault trace from Sorel because it is underlined by the dolomitized breccias. In this area, our mapping does not much differ from the previous ones proposed by the Sorel (1976) and Underhill (1989).

On the eastern part of the Argostoli basin, we did not find any evidence of the Aenos thrust with our mapping. The landscape is much smoothed and the post Piacenzian age of thrusting proposed by Underhill (1989) is questionable. However, if this structure had been active, it would have been during the lower Pliocene compressive event. However we kept this presumed fault on our map (see Fig. 2) because it can explain the absence of Eocene levels on the hanging wall while they outcrop in the footwall (the Minies Anticline).

To end, we notice that the placing of Krani Hill right over Koutavos lagoon is difficult to explain, and might have resulted from a rock slide that started from a crown scarp located uphill up to 160 a.s.l. This hypothesis is sustained by the fact that the dip distribution on the hill is extremely scattered. It is not clear if this hypothetical 'olistolith' is covered by the Quaternary infilling of Koutavos lagoon or partly overlaps the Quaternary, a fact that would explain the significant flow of the spring located at the water pump by Koutavos Park).

Following this field study, investigations were performed such as reinterpretation of pre-existing water boreholes, and acquisition of geophysical measurements (i.e., ambient vibration arrays, HVSR profiles). In June 2015, four boreholes were drilled in the Koutavos area, and several accelerometers were installed on surface and at different depths. The deepest borehole was cored to perform geological descriptions and characterization. Moreover, X-ray analysis and dating were performed on the collected samples from this borehole; results of these investigations are detailed below.

2.2. Results from new boreholes in the Koutavos park

Four boreholes were drilled in 2015 to install a permanent vertical accelerometer network in Koutavos park, to the southeast of Argostoli (green square symbol in the zoom of the Fig. 5). ARGONET consists of a vertical seismic array and a nearby (i.e., 440 m away) free-field station on bedrock (Theodoulidis et al., 2018a).

A detailed study was conducted at the ARGONET site, in Koutavos Park, close to the town of Argostoli (see Fig. 5). As a first step, several boreholes were drilled at the site: two deep boreholes; one cored borehole at 84.5 m (B1); one destructive borehole at 83.4 m (B2 also called BK0 in the cross sections descriptions) where a probe was installed; and three destructive boreholes at 40.1 m (B3), 15.5 m (B4) and 5.6 m (B5) in depth, very close to the first one (B2). The boreholes were drilled into the Plio-Quaternary units, and the deep borehole almost reached the Cretaceous limestone. A SPT was performed in B1. Two cross-hole and two down-hole measurements were also conducted: cross-hole (CH1) (between B2 and B3) and CH2 (between B3 and B4); and down-hole (DH1) in B2 and DH2 in B3. All these results are reported in (Theodoulidis et al., 2018a). The lithology description in Borehole B1 is shown in Fig. 3 as well as various indexes of the depositional environment of different units which are described below from bottom to top:

- **Unit *C***, which corresponds to Cretaceous limestone fragments that were collected at the bottom of borehole B1. These suggested that this unit might be reached a few meters below the bottom of the borehole, probably around 90 m below the surface, according to geophysical investigations (see Section 3).
- **Unit *Pa***, is probably lacking or very thin because of the aforementioned Cretaceous fragments found in the *Pb* formation at the bottom of the borehole.
- **Unit *Pb***, which is represented by a stiff material with marly sandy limestone and claystone from 68.2 m to the bottom (84.5 m) of borehole B1. This unit is also observed in two pre-existing boreholes that had been drilled about 1.5 km to the NW of Koutavos, close to the 'De Bosset' bridge (Fig. 2; see Rovithis et al., 2014).
- **Unit *Pt-k***, which is the 'soft' clays and sands. The detailed lithology here is presented in the description of the Koutavos borehole. This unit shows three distinct lithological main sets of clays from the top to the bottom: 28 m of red-brown clays with sand; 21 m of alternations of red-brown clays with marls and silts; and 10 m of gray-blue marls with organic matter and fossils (i.e., corals, gastropods, oysters). Some corals and shells were collected during the drilling, and they were characterized by X-ray diffraction and dated by the U-series method (see Section 2.3).
- **Unit *H*,** Holocene deposits are composed of about 6 m of lagoonal sediments, clayey silty sands to silty clays overlain by 2 m of backfill (clays and silty sands incorporating locally artificial deposits as rubbles).

The comprehensive description of the geotechnical parameters collected in these boreholes is presented in Theodoulidis et al., 2018a paper.

2.3. Coral dating and sediment mineralogy

To date, the Koutavos basin has been assumed to belong to the Quaternary era (Protopapa et al., 1998; Sorel, 1976; Underhill, 1989) without any dating to confirm this assumption. The cored borehole described in the previous section provided the opportunity to perform absolute dating, as fossils corals were found during the drilling.

Three samples (coded #6959, #6960, #7105) of fragment branches of corals that were coated in clay that filled all of the interstices and voids of the corallites, including the septa interstices, were collected from the core of borehole B1 at the base of the Pt-k lithostratigraphic unit (Fig. 4a), at 60.15 m and 63.00 m in depth. These corals may be *Lophelia pertusa* or Claedocora caespitosa that are common in Mediterranean Sea. In samples #6959 and #6960, the clay fraction was removed using a brush, followed by ultra-pure water washing. For sample #7105, an additional step using abrasion with a micro diamond saw was used. X-ray diffraction analysis was performed on the bulk sediment to determine the overall mineralogy, on the < 2 μm fraction for the clay composition, and on the cleaned and poorly cleaned coral fragments.

The bulk sediment had a mineral composition that was typical of shallow marine environments, as a mixture of calcite, clay, evaporite, and detrital components. The clay composition was 71% to 74% smectite, 17% to 18% illite, 6% to 8% chlorite, and 2% to 4% kaolinite. This clay composition is typical of temperate climates, such as the Cephalonia climate in the present time. However, the presence of gypsum in the bulk sediment and corals implies some periods of aridity with a slight decrease in the sea level, which may have resulted in some evaporite deposits.

In order to select pristine samples suitable for dating, the mineralogical composition of the coral samples was estimated following the method detailed by Sepulcre et al. (2009). The constitutive minerals of samples #6959 and #6960 were, in order of abundance: aragonite, quartz, calcite, vermiculite, muscovite, and gypsum. Sample #7105 was 100% aragonite. For the U-series analysis, the detailed U—Th separation and purification protocol can be found in (Pons-Branchu et al., 2014). Table 1 gives the U, Th, isotopic ratios, and ages. The U content showed little variation (from 2.64 ± 0.01 to 2.75 ± 0.004 ppm), while ^{232}Th and ^{230}Th/^{232}Th showed larger variations (from 33.7 ± 0.3 to 348.1 ± 1.2 ppb, and 25.8 ± 0.1 to 245.6 ± 1.8, respectively). The δ^{234}U were close for the three samples, although slightly higher for the purest (100% aragonite) sample (#7105). The ages were corrected for initial ^{230}Th, assuming an initial ^{230}Th/^{232}Th activity ratio of 7 ± 50%, and taking into account the decay of this initial ^{230}Th with time. The corrected ages were not very different from the uncorrected ages, and were 411.8 ± 46.17 ka for the 'clean' sample (#7105), 539.93 ± 101.03 ka for the sample with remaining clay (#6960). Sample #6959 that was very rich in clay content had an apparent age out of the ^{230}Th/^{234}U dating limits.

Diagenesis is a major issue for the dating of fossil corals, as it can

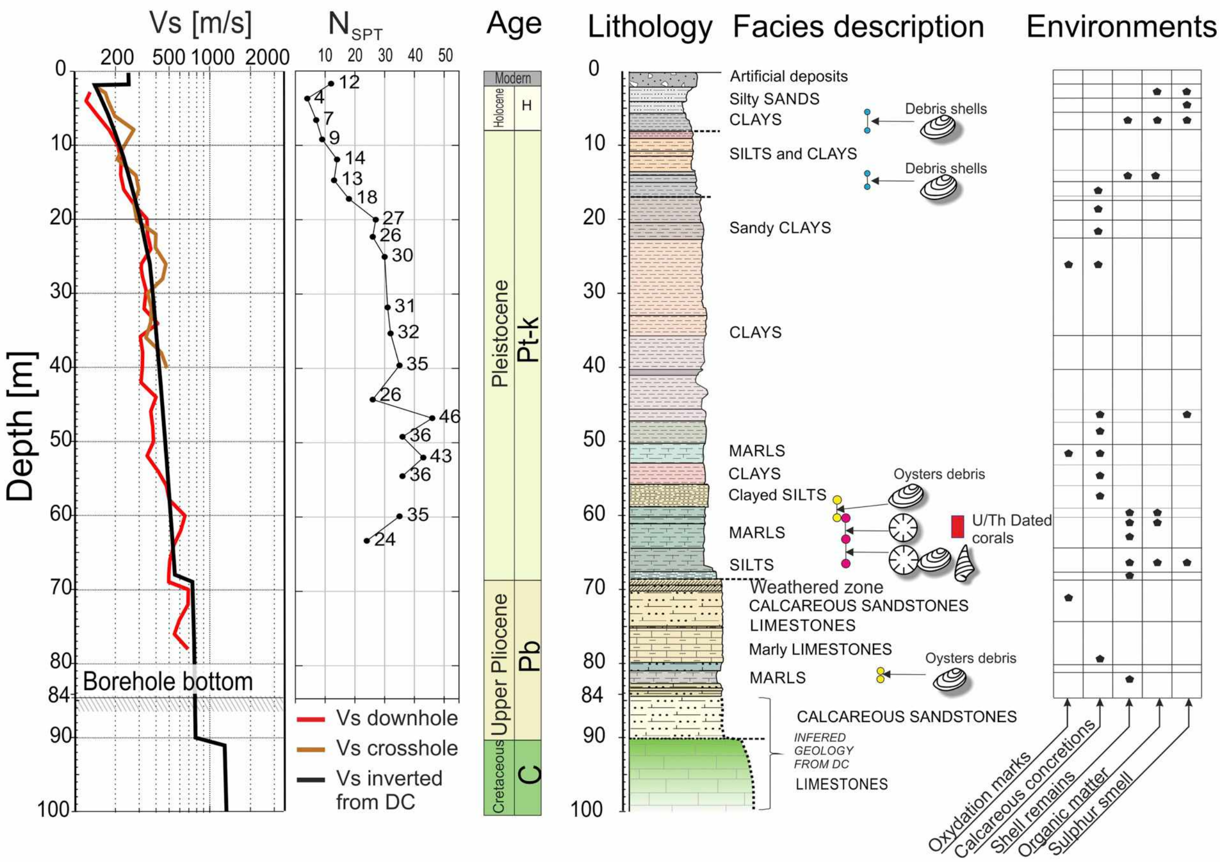

Fig. 3. Koutavos borehole (B1) with facies description, environments, and Standard Penetration Test (SPT) measurements and *Vs* values.

cause U and/or Th loss and/or gain (open system behavior), which will result in biased ^{230}Th/^{234}U ages (e.g., (Pons-Branchu et al., 2005). Moreover, these effects are time dependent, and the probability of the opening of a system increases with time (Villemant and Feuillet, 2003). The identification of diagenetic processes is mainly based on examination of the alteration in the initial coral mineralogy, with identification of calcite in aragonitic species and the high ^{232}Th, which indicates alteration or contamination. On the contrary, a fossil coral analysis with a $\delta^{234}U_0$ value within the range of present-day seawater ± 20‰ is assumed to have remained in closed system (Andersen

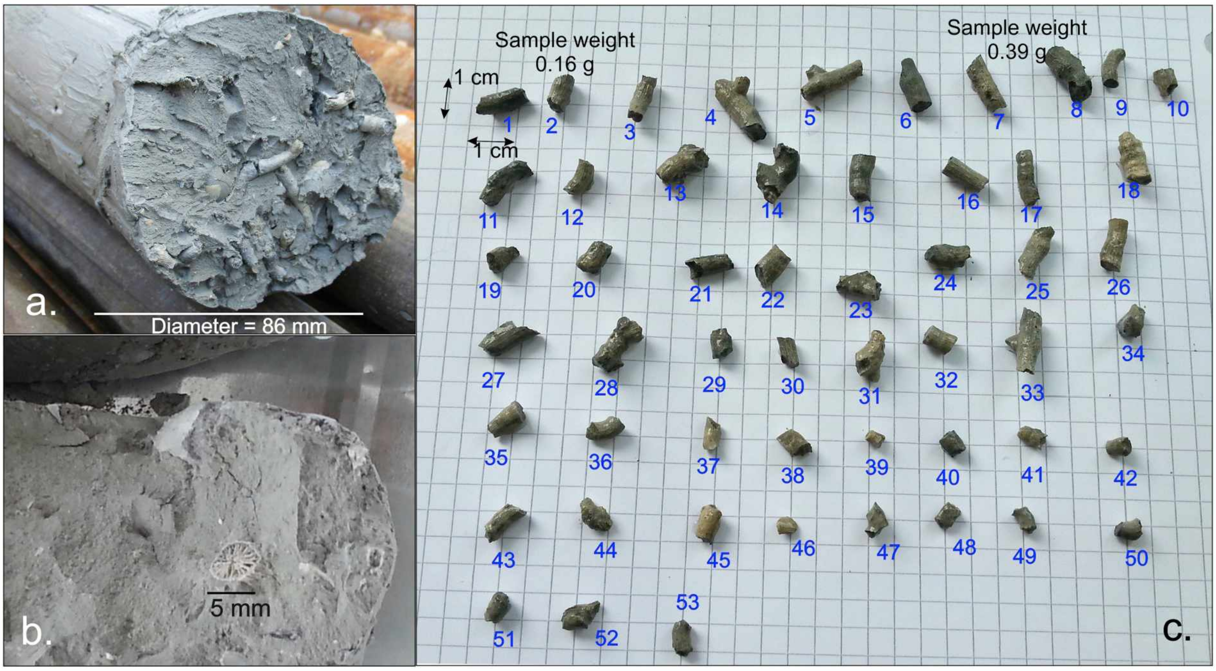

Fig. 4. Preserved coral debris collected for dating. (a) Coral debris extracted from borehole B1 (core sample between 59.7 m and 63.9 m in depth). (b) Transverse section of the core, showing coral polyps. (c) All of the collected coral debris for dating, with weight examples and size scale.

Table 1
U, Th, isotopic ratios, and ages of the coral samples from the core of borehole B1 at the base of the Pt-k lithostratigraphic unit.

Sample	$[^{238}U]$ (ppm)	$\delta^{234}U_m$	$^{230}Th/^{232}Th$	$[^{232}Th]$ (ppb)	$^{230}Th/^{238}U$	Age (ka B.P.)	Core age (ka B.P.)	$\delta^{234}Uo$
#6959	2.64 ± 0.01	31.82 ± 0.85	25.8 ± 0.1	348.1 ± 1.2	1.04 ± 0.012	sup 500		
#6960	2.75 ± 0.004	31.72 ± 1.22	90.2 ± 0.3	102.9 ± 0.3	1.03 ± 0.007	546.74 ± 103.34	539.93 ± 101.03	145.95 ± 42.05
#7105	2.67 ± 0.02	36.04 ± 2.5	245.6 ± 1.8	33.72 ± 0.3	1.02 ± 0.007	414.27 ± 45.84	411.80 ± 46.17	116.02 ± 17.03

Core age, corrected ages for the detrital fraction.
δ^{234}Um = ({$^{234}U/^{238}U$}measured/{$^{234}U/^{238}U$}equilibrium - 1) × 1000, with $^{234}U/^{238}$Uequilibrium = 54.89 × 10–6 (molar ratio, Cheng et al., 2013).
$\delta^{234}U_o$ is $\delta^{234}U$ at the initial time (using the $^{230}Th/^{234}U$ ages).

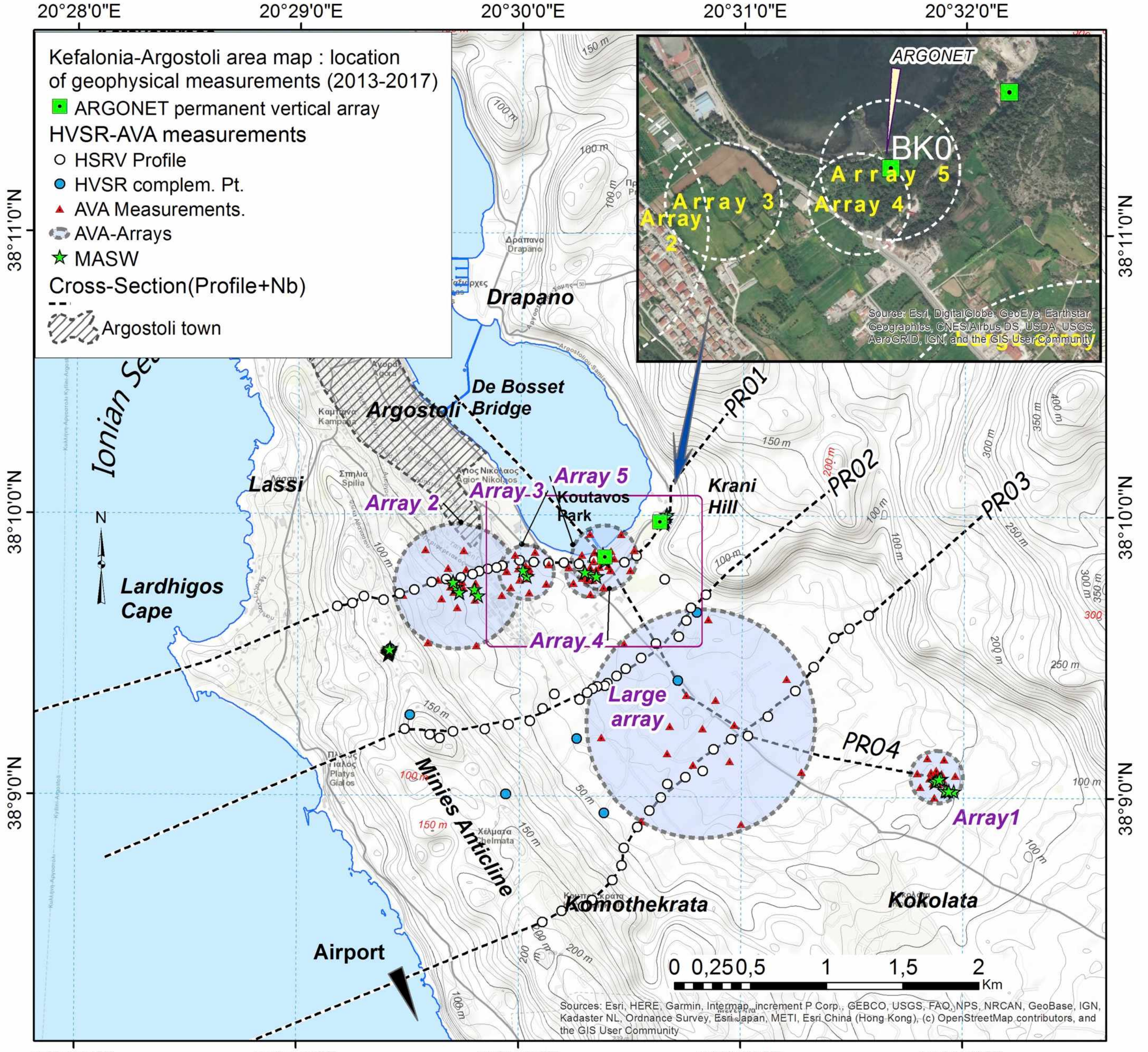

Fig. 5. Location of SWDA measurements during both 2013 and 2017 campaigns (Ambient Vibration Arrays, HVSR and MASW). HVSR were performed along the 3 profiles (PR01 to PR03). The Profile 04 starts from a 'rock site' to Koutavos ARGONET borehole and De Bosset Bridge. The 4 profiles are used in Section 4.2 to construct geological sections. Six AVA were performed: Array 1 (rock site), Array 2 (Pliocene site), Array 3 (west of Koutavos), Array 4 (center of Koutavos), Array 5 (ARGONET) and Array 6 (Large array). MASW measurements were located within the arrays and additional measurements were performed on rock sites. Location of the permanent ARGONET sensor array (vertical array + free-field station on bedrock) is also indicated.

et al., 2008). Accordingly, these Cephalonia corals reached the two classical criteria for age validity (i.e., aragonitic structure, $\delta^{234}U_0$ compatible with modern sea water uranium isotopic composition ± 20‰). The data from sample #7105 represents the most confident age (i.e., better clay removal before analysis and 100% aragonite).

Regarding dating and mineralogy, the fossil corals (see Fig. 4b and c) certainly corresponded to a high-stand and warm period. Looking at the marine isotopic stages deduced from the records of $\delta^{18}O$ and sea level curves (Lisiecki and Raymo, 2005), these fossils might have been contemporaneous with the MIS 11 high stand (~420 ka), based on the possible age range given by samples #7105 (with greater confidence) and #6960, and that the clay composition around the corals was typical of a temperate climate. In this way, the limit between *Pb* and*Pt-k* would match with the stratigraphic limit between the Calabrian and the Ionian, and would correspond to the unconformity that followed the major deformation episode in the pre-Apulian domain that formed the Minies anticline. Considering the dating of the coral cored at 63 m in depth, the consequence is that the Argostoli/ Koutavos syncline is still active and has led to the Koutavos marsh subsidence. Thus, considering for regular subsidence and that the 420 ka high stand is equivalent to the present sea level (Bowen, 2010), and that the occurrence of evaporites and of corals are associated to a shallow water depth, this implies that the mean local subsidence rate in Koutavos is about 0.15 mm/ yr or more. One note that this subsidence rate is the same magnitude order that one could be determined on the raised beaches located North of Mines Village (see Section 1.2).

3. New information from the geophysical surveys

To obtain new information about the geometry of the Argostoli basin and to measure shear wave velocity (V_S), required in 3D models, two geophysical surveys were carried out in September 2013 and October 2017. These surveys involved single-station ambient vibration measurements for horizontal-to-vertical spectral ratio (HVSR) analysis (Nakamura, 1989; SESAME team, 2004; Bard et al., 2010), as well surface-wave dispersion analysis (SWDA) technique (Foti et al., 2018).

The SWDA includes the measuring of the phase velocity of the surface waves (Rayleigh and/or Love waves) as a function of the frequency, to determine the dispersion curves. These dispersion curves are then converted into V_S profiles using an inversion algorithm. To obtain a dispersion curve over a satisfactory band width (i.e., to derive a V_S profile with sufficient resolution and investigation depth), two acquisition methods were used. For high frequencies (i.e., short wavelengths, and hence shallow investigation depths), we used the ‘multichannel analysis of surface wave’ (MASW) measurements in which geophones are placed along a line and surface waves are generated by hitting the ground with (for example) a sledge hammer. For lower frequencies (i.e., larger wavelengths, and hence deeper investigation depths), we used the ambient vibration array (AVA) technique, with sensors placed in consecutive circles of increasing apertures, plus one sensor in the center. In this case, we estimate the phase velocity of the surface waves that are contained within the ambient vibration wavefield. The 2D feature of the array allowed the identification of the propagation direction of the surface wave trains, which is mandatory to estimate velocities. The SWDA acquisitions were carried out in six areas (Fig. 5: Array 1+ Array 6, to characterize the bedrock velocity profile; and Arrays 1 to 4 along PR01 profile, to characterize the velocities within the Argostoli basin). All of the individual sensor recordings from the SWDA were also processed as single-station HVSR measurements. The HVSR and SWDA measurement locations are shown on the map of the Fig. 5 and are specified in the Appendix- Table A.1.

Basically, the HVSR method consists of computing the Fourier spectra of ambient vibration recordings, and plotting the ratio of the horizontal to vertical spectra. This analysis is done over many time windows, and a mean is computed to provide the final HVSR curve. This curve often shows one peak, which is an indication of the presence of a contrast within the V_S velocity profile below the measuring point. The frequency of this peak, denoted as f_0, indicates the fundamental resonance frequency of the soil column, and it is mainly conditioned by the depth (h) of the velocity contrast and the value of V_S between the surface and the velocity contrast ($f_0 = V_S/4\,h$ in the simplified case of a single homogeneous layer overlying an homogeneous half-space). The f_0 value can therefore provide indirect information about the depth of geological interfaces. The HVSR analyses were carried out along three profiles (see Fig. 5: PR01, PR02, PR03), which were roughly perpendicular to the syncline axis, and at a few complementary points corresponding to key locations for our integrated interpretation (e.g., locations of available borehole information).

3.1. Surface wave dispersion analysis

Six areas were investigated by Ambient Vibration Arrays named as Array 1 (rock site), Array 2 (Pliocene site), Array 3 (west of Koutavos), Array 4 (center of Koutavos), Array 5 (ARGONET) and Array 6 (Large array) (see Fig. 5). Each acquisition involved 15 sensors for AVA measurements (Güralp CMG6TD broadband seismometers with integrated digitizer. This number of sensors allowed the use of double-circle geometry (one sensor in the center; 2× seven sensors equally spaced around two circles). The azimuth of the sensors for the larger circle was shifted by ~26° (360°/14) with respect to the azimuth of the sensors for the smaller circle, to optimize the azimuthal coverage of the whole array. A radius ratio of 3.0 was chosen for the increase between the two consecutive array radii. For consecutive acquisitions, the inner/ smaller circle was moved to form the next larger circle. The whole data acquisition for each array last about few hours. This kind of geometry has also been used in several other characterization surveys (Hollender et al., 2018). The MASW measurements were performed within the Arrays 1 to 5 and on two rock site locations (see Fig. 5).

For Array 1 (rock), three sets of layouts were used, with increasing paired radii of: 5 m and 15 m; 15 m and 45 m and 45 m and 135 m. The site was selected to the south-east of the Argostoli syncline, on an outcropping area of karstified Cretaceous limestone (*C*) with a relatively flat topography and low layer dip. This site was also chosen for the ‘dense velocimeter array’ of the Sinaps@ post-seismic survey (Imtiaz et al., 2018; Perron et al., 2018; Svay et al., 2017).

For the ‘Large array’, a single layout was used, with paired radii of 230 m and 700 m. This array was deployed within the Argostoli syncline, where the Holocene and Pleistocene formations were outcropping, to take advantage of a wide flat area. However, considering the reduced thickness of the overlying formations and the very large array aperture, the objective of this acquisition is the evaluation of the velocity in the Cretaceous limestone (*C*) bedrock at large depth. The dispersion curves deduced from this array can be combined with those of Array 1 (rock) to obtain the reference velocity profile within the bedrock down to a large depth.

For Array 2 (Pliocene), four sets of layouts were used, with increasing paired radii of: 5 m and 15 m; 15 m and 45 m; 45 m and 135 m and 135 m and 405 m. This array was deployed to the west of Koutavos Park where the Pliocene stiff formation (*Pb*) is outcropping. This array was designed to determine the reference velocity profile within the *Pb* formation.

For Array 3 (west of Koutavos), three sets of layouts were used: 7 m and 20 m; 20 m and 60 m and 60 m and 180 m. This array was deployed to the west of Koutavos Park, where the Pleistocene formation (*Pt-k*) is outcropping. The location of this array was chosen so as to better constrain the velocity profile where the ‘double peak’ HVSR response can occur.

For Array 4 (center of Koutavos), three sets of layouts were used: 5 m and 15 m; 15 m and 45 m and 45 m and 135 m. This array was deployed within Koutavos Park.

Finally, Array 5 (ARGONET) was deployed using the ARGONET accelerometric station as the center. Three sets of layouts were used:

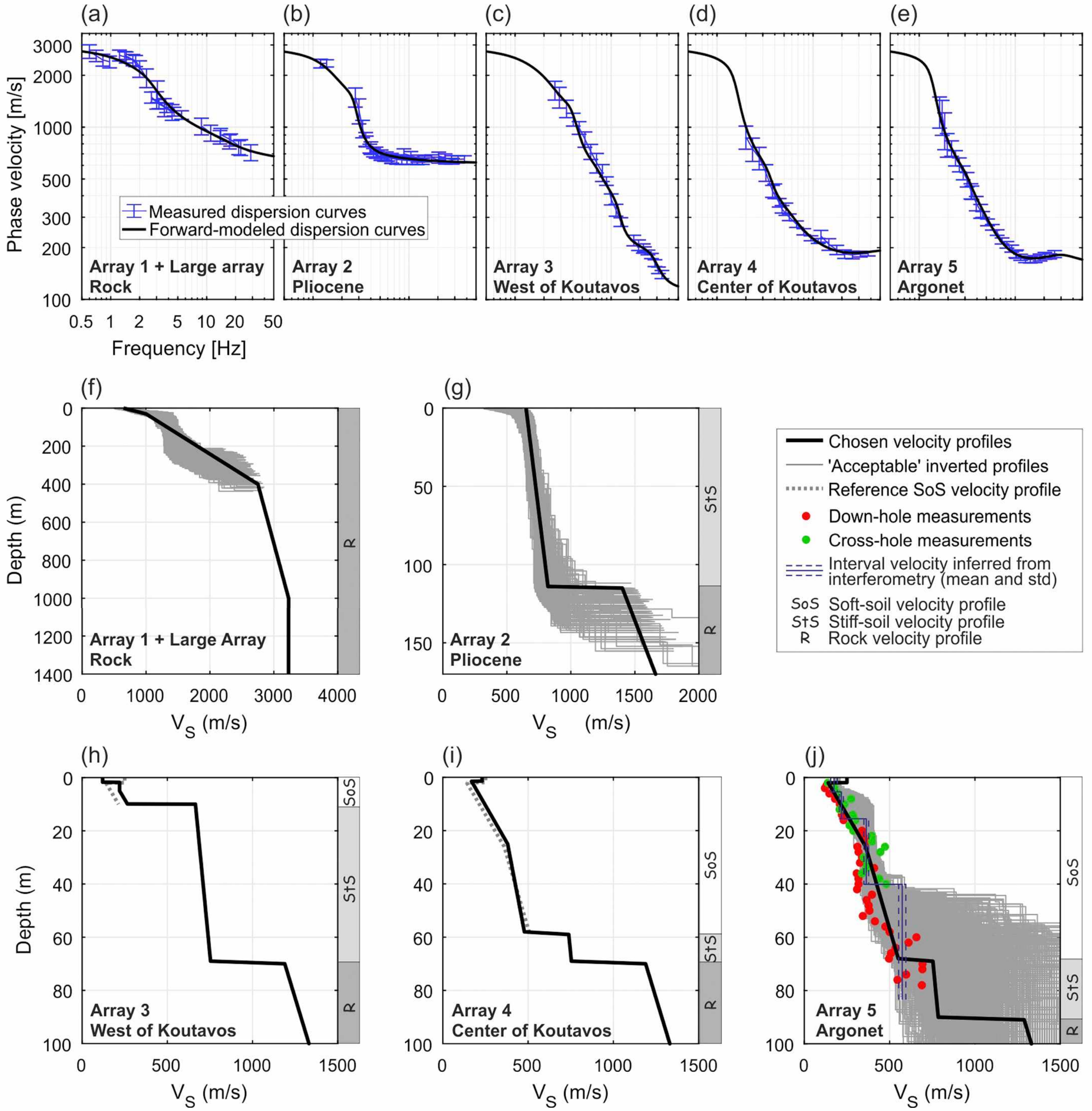

Fig. 6. Results of the surface wave dispersion analysis survey processing. (a-e) Measured dispersion curves and associated standard deviation (blue) and forward-modeled dispersion curves (black) for all of the arrays. (f-j) Derived shear-wave velocity profiles: simplified model (black); 'acceptable' inverted profiles (gray, thin solid lines); reference soft soil velocity profile (corresponding to the best solution for array 5) for comparison of those obtained for arrays 3 and 4 (gray, thick dashed line). (j) Other sources of V_S data obtained at the ARGONET site: cross-holes (green points), down-holes (red points) and seismic interferometry (blue lines). (f-j) Columns on the right of these velocity profile plots show the depth range of the three reference velocity profiles used (**SoS**, soft soil; **StS**, stiff soil; **R**, rock). (For interpretation of the references to color in this figure legend, the reader is referred to the web version of this article.)

9 m and 27 m; 27 m and 80 m and 80 m and 240 m. This array was also located within Koutavos Park, where the Holocene formation (*H*) is outcropping, and it provided the reference velocity profile for the *H* + *Pt-k* formations.

SWDA analysis included the application of: (1) the frequency-wavenumber (FK) (Neidell and Taner, 1971; McMechan and Yedlin, 1981; Douze and Laster, 1979); and (2) the modified spatial autocorrelation (MSPAC) (Bettig et al., 2001; Köhler et al., 2007) methods for the AVA datasets and the FK method for the MASW data. More details about the processing can be found in Hollender et al. (2018). Only the vertical component was analyzed, i.e., focusing on Rayleigh waves. The dispersion curves that corresponded to the fundamental mode of the Rayleigh wave obtained for each array are shown inFigs. 6a to 6e. The results from Array 1 and the Large array are shown on the same plot (Fig. 6a). Array 1 + Large array allows a dispersion curve to be obtained from 0.5 to 30 Hz; Array 2, from 1 to 40 Hz (Fig. 6b); Array 3, from 2.5 Hz to 35 Hz (Fig. 6c); Array 4, from 2.5 to 40 Hz Fig. 6d); and Array 5, from 1.5 to 30 Hz (Fig. 6e).

The inversions were performed with the inversion tool of the Geopsy software package, which uses a global search approach with a neighborhood algorithm (Wathelet, 2008). Previously derived broadband dispersion curves that corresponded to the Rayleigh wave fundamental mode were inverted to V_S profiles. The f_0 values determined by HVSR were also used in a joint inversion for Array 2 to Array 5. We used the 'acceptable misfit' approach (Lomax and Snieder, 1995; Souriau et al., 2011), which led to a set of equivalent V_S profiles that explained the dispersion estimates within their uncertainty bounds. In such a case, the search algorithm did not try to find the best misfit V_S profile, but rather a large number of V_S profiles that explained the data equally well. These obtained profiles are shown on Fig. 6f, g and j, as light gray lines.

Within the objective of producing simplified velocity models in the perspective of performing the first 3D numerical simulations of ground motions, we propose simple V_S 'laws' as a function of depth. These simplified velocity profiles do not aim to represent a real description of the properties of the area: the description of lateral heterogeneities and uncertainty assessments are not addressed here. However, we aimed to propose models that were compatible with the available information, as the dispersion curves and HVSR f_0 values, as well as the borehole geological descriptions, cross-hole and down-hole measurements performed for the ARGONET boreholes, and the V_S valuesobtained by seismic interferometry using seismological data recorded by the ARGONET vertical array.

The velocity profile proposed for the bedrock is assumed to be applicable to both Cretaceous limestone (*C*) and Pliocene sandstone and breccia (*Pa*) because of their apparent mechanical strength. This model is based on the dispersion curves obtained by the 'Rock' and 'Large' arrays (**R** [rock] reference velocity profile), and it can be expressed as:

$$V_S(h) = \begin{cases} 11.7h + 650, \ 0 \leq h \leq 30 \\ 4.7h + 858, \ 30 < h \leq 400 \\ 0.8h + 2430, \ 400 < h \leq 1000 \\ 3230, \ h > 1000 \end{cases} \tag{1}$$

where V_s is the shear-wave velocity (expressed in m/s) and h is the depth below the ground surface (expressed in m). The value of 3230 m/s below the depth of 1000 m allows this velocity model to be joined to that proposed by Haslinger et al. (1999) for greater depths. In Fig. 6f, this model (black line) is compared to the 'acceptable profiles' derived from the empirical dispersion curves inversion (Fig. 6f, light gray lines). The forward-modeled dispersion curves computed with this velocity model are also compared to the empirical ones in Fig. 6a.

The velocity profile proposed for the Pliocene sands and sandstone formations (*Pb*) (**StS** [stiff soil] reference velocity profile) can be expressed as:

$$V_S(h) = 1.5h + 650 \tag{2}$$

This relation is only suitable down to the bottom of the *Pb* formation. Beneath this, the relation of the **R** model (eq. [1]) should be used. Fig. 6g compares this hybrid (**StS** and **R**) model with the 'acceptable profiles' obtained from Array 2. Here the contact between *Pb* and the underlying *Pa* + *C* formations is located at 115 m in depth. Below this depth, the bedrock velocity model was used. The forward-modeled dispersion curve is compared to the empirical ones presented on the Fig. 6.

As for the determination of a velocity model within the formation of Koutavos Park (i.e., *Pt-k, H*), several sources of information are available. The first information source is the dispersion curve obtained from Array 5 (ARGONET – centered array). The second source of information is the cross-hole and down-hole measurements performed within the ARGONET boreholes before the installation of the accelerometers. Cross-hole (resp. down-hole) measurements are available within the 2 m to 40 m (resp. 3 m to 78 m) depth interval (colored points in Fig. 6j). Additionally, based on the use of the ARGONET events database (386 events for July 2015 up to April 2017; Theodoulidis et al., 2018a) it was possible to evaluate the mean V_S within the intervals defined by the locations of consecutive sensors using a seismic interferometry approach (for more details on the methodology, see methodology sections of, e.g., Chandra et al. (2015) and Guéguen (2016). For the 0 m to 5.6 m, 5.6 m to 15.5 m, 15.5 m to 40.1 m, and 40.1 m to 83.4 m intervals, the corresponding values obtained were 174 ± 19 m/s, 217 ± 12 m/s; 363 ± 14 m/s, and 574 ± 21 m/s, respectively. Considering the interferometry data as the reference, in the present study, the cross-hole measurements overestimate the velocities by 5% to 10%, whereas the down-hole measurements underestimate them by 10% to 15%. These differences between the two invasive geophysical methods have the same order of magnitude to those given by Garofalo et al. (2016) for other sites within the framework of the InterPacific project. The available lithological log made on the basis of the analysis of the geological cores also helped to identify the exact position of the *Pt-k/Pb* limit at 69 m in depth. The simplified model within the formations (*Pt-K* + *H*) (**SoS** [soft soil] reference velocity profile) is fully compatible with the interferometry velocity values and is compatible with the cross-hole and down-hole measurements (taking into account their respective bias), and can be expressed as:

$$V_S(h) = V_S(h) = \begin{cases} 250, \ 0 \leq h \leq 2 \\ 9.2h + 122, \ 2 < h \leq 26 \\ 4.5h + 242, \ h > 26 \end{cases} \tag{3}$$

This model is illustrated in Fig. 6j, where the *Pt-k/Pb* limit is fixed at the depth of 69 m and the *Pb/C* interface is assumed to be at 90 m in depth (the velocity profile between 69 m and 90 m in depth is, hence, deduced from eq. [2] and below 90 m in depth from eq. [1]). The forward-modeled dispersion curve derived from the use of the hybrid model of Fig. 6j is compared to the empirical one in Fig. 6e.

The velocity profiles derived from Array 3 and Array 4 are shown in Fig. 6h and i, respectively. The corresponding forward-modeled dispersion curves are compared to the empirical ones in Fig. 6c and d. For Array 3, the limit between the *Pt-k* and *Pb* formations (resp. between the *Pb*and *Pa*+*C* formations) was at 10 m (resp. 70 m). For Array 4, the limit between the *Pt-k* and *Pb* formations (resp. between the *Pb* and *Pa* + *C* formations) was at 58 m (resp. 69 m). Note that the optimal velocity profile within the *Pt-k* (or *H* + *Pt-k*) formation did not fit the **SoS** reference velocity profile perfectly, although the differences remained relatively small. This is shown in Fig. 6h and i where the optimal velocity profiles obtained are presented in black, whereas the reference **SoS** profile (as defined at ARGONET location and expressed in eq. [3]) is plotted as gray dashed line.

The **StS** (resp. **SoS**) reference velocity profiles derived from the SWDA results were also used to deduce the upper and lower bounds for the depth of the *Pb/Pa* (resp. *H* + *Pt-k/Pb*) limit. Using the HVSR f_0 values at the array centers and the f_0 values from all other HVSR measurements, the corresponding limits of the upper and lower bounds were deduced and then used for building the Argostoli basin cross-section. The complementary values of f_0 away from those of the cross-sections (e.g., all available measurements on each AVA) were also used to complete the interface depth to constrain the interpolation in the 3D model (see Section 3.2).

3.2. HVSR analysis and interpretation

The HVSR processing was performed using the Geopsy software (Wathelet, 2008) following a standard procedure (SESAME team, 2004) that was designed for HVSR ratio curve computation in different azimuths. The significant polarization of most of the HVSR points showed a preferential direction of about N140E, which corresponds to the axis of the syncline.

A first analysis of the HVSRs aimed to sort them in terms of curve

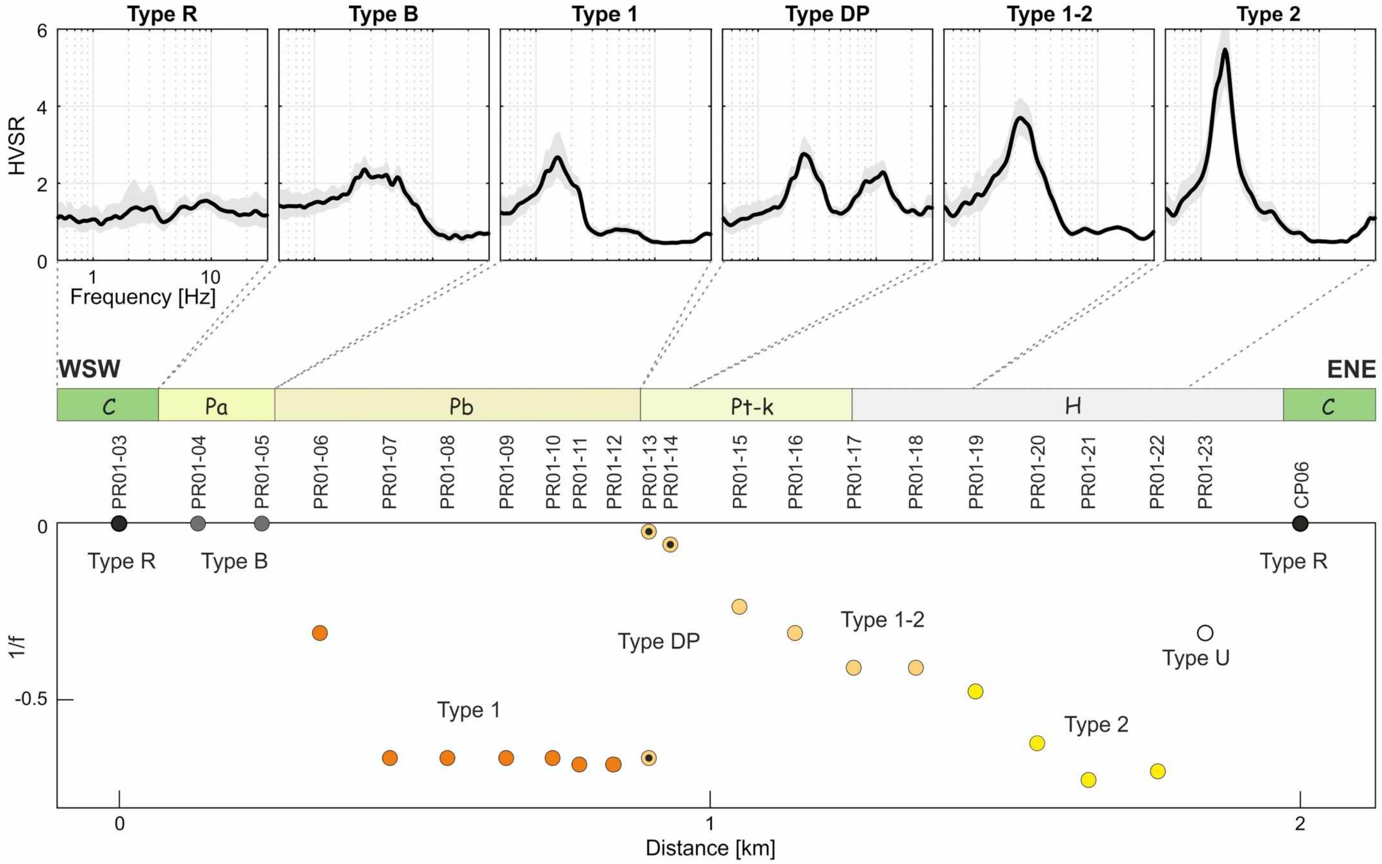

Fig. 7. Top: Identification of the six typologies of the HVSR curves. Center: Correspondence with the outcropping geological formations. Bottom: First-order qualitative and unscaled representation of the possible depths of the contrasts that cause the HVSR peaks (inverse of the frequency f_0 and f_1). When no frequency was picked, the points were plotted as if they had an infinite f_0. The horizontal axis follows profile PR01, using point PR01–03 as origin (left-most point).

typologies. Several groups were defined (Fig. 7):

- Type 1: relatively broad, but still with a clear peak, with relatively small amplitude (< 3);
- Type 2: narrow and very clear peak, with relatively large amplitude (> 5);
- Type 1–2: intermediate typology between Type 1 and Type 2;
- Type DP (Double Peak): points showing two relatively clear peaks with the lower frequency peak usually from Type 1;
- Type B: unclear and very broad 'bump' (no identifiable f_0), but with an amplitude that can be > 2;
- Type R: almost flat HVSR response, and usually assumed to be a 'rock site';
- Type U: a few points that cannot be associated to one of the former types, and hence that are qualified as 'undefined'.

The fundamental frequency (f_0) values were extracted from the HVSR curves of Types 1, 2, 1–2, DP, and U when a peak allowed frequency identification. The second identifiable frequency (f_1) values were extracted from HVSR curves of Type DP. All of these frequency identifications were performed, as mentioned earlier, using the HSVR curves computed for azimuth 140°.The DP feature is interpreted for structural interpretation in the further Section 4.1 and compared to theoretical computing in Fig. 8.

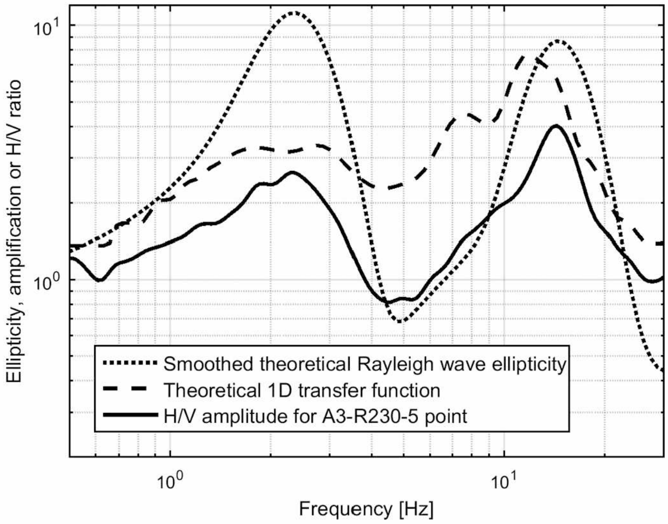

Fig. 8. Double peak of the HVSR measurements at point A3-R230–5, compared to the theoretical Rayleigh wave ellipticity and the theoretical 1D SH transfer function for a shear-wave velocity profile consistent with the geology and other geophysical information (e.g., shallow interface between soft Quaternary and stiff Pliocene, deeper interface between stiff Pliocene and rock).

4. Steps to build the geological model and discussions

This study provides a general methodological interest through the implemented multidisciplinary coupling, which integrates geological mapping, geotechnical borehole characterization, dating and geophysical measurements based on the analysis of the surface wave dispersion. It allows to precise and control the 3D geometry and engineering features of sedimentary basin prone to site effects. Generally, the characterization of basins is based on microzonation leading to fundamental frequencies mapping, often based on single station broad band of ambient vibration measurements (e.g. in Slovenia: Gosar, 2007; Mississipi basin: Bodin et al., 2001, Guo et al., 2014, Guo and Aydin, 2016). This has been performed using the Nakamura method (Nakamura, 1989). HVSR curves are generally used to estimate the fundamental resonance frequency (f_0) of basins (see e.g. Bard et al., 2010; Perron et al., 2018). Further on, coupling ambient vibration and sometime, geological context (geological log and/or geotechnical characteristics of soft layer for example) were more recently performed, thanks to the availability of dispersion curves processing inversion approaches (e.g. Wathelet, 2008). Even if the interpretation of a given measurement and often 'locally' performed in 1D, the multiplication of measurements over an area could lead to 2D to 3D information (cross section or volumes) encompassing V_S profiles from surface to bedrock. The approach is often mainly based on a geophysical-geotechnical approach, using class of soils (e.g. EC8 soil classes, EUROCODE8, 1998), providing vertical velocity profiles or V_{S30} for engineering purpose (eg. Borges et al., 2016 in portugal). Some few studies also address more specifically the geological context based on geological maps or cross section (e.g. Akyol et al., 2013 in Turkey). Some others combine geotechnical investigations (Gouveia et al., 2016 in Portugal, Saroli et al., 2020) or other geophysical methods (active or passive) such as electrical resistivity tomography (Gosar, 2007 in Slovenia; Sauret et al., 2015 in Burkina Faso;), gravimetry (e.g. Özalaybey et al., 2011 in Turkey; Martorana et al., 2018 in Sicilia) or and seismic investigation such as reflexion/ refraction HR investigations (e.g. Gosar et Lenart, 2010 in Slovenia). More comprehensive studies aiming to construct 3D geological/ geotechnical/ geophysical model have been developed (e.g. Manakou et al., 2010 for the Mygdonian basin in Northern Greece; Eker et al., 2015, Pamuk et al., 2018 in Turkey; Podestá et al., 2019 in Chile).

In this paper, we propose a combined geological/ geotechnical/ geophysical process. The complementarity of these methods is not limited to the aggregation of data of different nature to provide a single final interpretation, once the different measurement surveys have been carried out independently. Indeed, at each step one discipline helps the other to design its experimental plans and interpret its results. In more details, the geological work allowed to locate properly the HVSR geophysical profiles. The analysis of the typology resonance peaks helped in drawing the outlines of the geological map. The geophysical results make it possible to better quantify the thicknesses of the different geological layers (and also to give quantified information on the V_S) to help in the elaboration of the four cross sections. From, each cross-section a set of control points was determined for each interface (i.e., x, y, z; where z is the elevation – or depth - with respect to sea level). The 3D geological model was then built combining interface limits of each cross-section and the complementary information (e.g., depth deduced from punctual HVSR measurements, borehole data, interface topographic position, formation limits on the geological maps). The next sections present and discuss this approach.

4.1. Contribution of the HVSR interpretation to the construction of the geological model

To interpret the HVSR typologies and to be able to link the f_0 interpretation to a specific geological contrast, a first comparison with the available geological information was performed along profile PR01. Fig. 7 shows a schematic drawing of this preliminary analysis, where the different types of HVSR curves, as well as quantities $1/f_0$ and $1/f_1$ for the DP typology, are plotted (first-order qualitative and unscaled representation of possible depths of contrasts causing the HVSR peaks). When no frequency was picked, the points at the bottom part of Fig. 7 were plotted as if they had an infinite f_0 (Types R, B). At first glance, when considering the f_0 value variation along the profile, a possible basin effect can be identified in the east part of the profile, between points PR01–13 and PR01–23. A second basin may also be suggested in the west part, between points PR01–06 and PR01–12. Making the assumption of two separated basins, the sharp transition between points PR01–12 and PR01–13 suggests a fault-like transition, although this assumption is not supported by geological observations. The most likely and geologically consistent interpretation involves the existence of a single basin, with two nested velocity contrasts.

Based on the comparisons between the HVSR typologies and the geological cross-section, we suggest that the contrast that produced the peak for Type 1 points is associated to the *Pb/Pa + C* contact. The hypothesis that the Type 1 peak might be due to the *Pa/C* contact was also addressed, but the outcropping observations do not support this hypothesis, as the *Pa* lithology clearly appears as a 'rock' formation (as for the *C* lithology), whereas the *Pb* lithology appears as a 'stiff soil' formation. We hence suggest that the *Pb/Pa* velocity contrast is higher than the possible *Pa/C* contrast, and hence it is more prone to produce a peak in the HVSR measurements. Similarly, we suggest that the peak for the Type 1–2 and Type 2 typologies is due to the *Pt-k/Pb* contrast (or more generally, the contrast between the *Pt-k + H* as a whole and the underlying formations, i.e., either *Pb, Pa* or *C*, depending on the HVSR location).

The double peak typology (Type DP) was observed only within a small area. To test if this double peak feature is caused by the presence of two velocity contrasts (i.e., *H + Pt-k/Pb, Pb/Pa + C*), we performed 1D numerical simulations using realistic velocity profiles deduced from the SWDA (see below), that were coherent with the geological information. On the one hand, we computed the theoretical shear-wave transfer function; on the other hand, we computed the Rayleigh wave ellipticity. Both of these phenomena may explain the origin of the HVSR peaks. The results of one of these simulation tests are shown in Fig. 8 and are compared to a measured HVSR curve (recorded at point A3-R230–5, see Table A.1). This test confirms that the double peak is probably due to the presence of two contrasts. Sensitivity tests showed that the double peak can be observed as long as the *H + Pt-k/Pb* interface remains relatively shallow (< 10 m). As soon as this depth increases, the first, lower frequency, peak (associated to the *Pb/Pa + C* contact) disappears and/or is absorbed by the second, higher frequency, peak associated to the *H + Pt-k/Pb* contact. This may explain why the area where the double peak is observed is relatively narrow.

This discussion leads to the following conclusions in terms of the use of HVSR typologies for geological interpretation. Type R' is associated to the *C* lithological formation (Cretaceous limestones); Type B is associated to *Pa* (Upper Pliocene sandstone and breccia); Type 1′ is associated to *Pb* (Upper Pliocene sands and sandstone); Type 1–2′ and Type 2′ are associated to the *H + Pt-k* as a whole; Type DP is associated to a *H + Pt-k* outcropping, but with shallow contact between *H + Pt-k* and *Pb*. Finally, Type 2 HVSRs often exhibit very large amplitude peaks (> 8), mainly within the eastern part of the basin. This could be explained by the fact that *H + Pt-k* is in direct contact with the *C* formation, which maximizes the velocity contrast, and hence the HVSR amplitude. These interpreted suggestions provide valuable support for optimization of the updated geological map. Kassaras et al. (2017) report seven double peaks in the northern continuity along the Koutavos and Argostoli bay shore. These points are located on the extension of the narrow band of double peaks highlighted in our study.

4.2. Two-dimensional geological cross-sections and geological map of the Argostoli basin

From the geological characterization and dating (see Section 2) and previous works (Sorel, 1976; Underhill, 1989), we propose on the Fig. 9 a spatial distribution (laterally evolving from Minies –West– to Koutavos area –East–) of the different stratigraphic units from the Cretaceous bedrock to the Quaternary deposits. More specifically, the new subdivision defined in Section 2 in the in the lower Pliocene to lower-middle Pleistocene series (*Pa, Pb* and *Pt-k* units) is used here.

This spatial distribution of the stratigraphic boundaries and a detailed mapping allowed updating the geological map the Argostoli area proposed in previous works (Fig. 10). Moreover, the fairly good

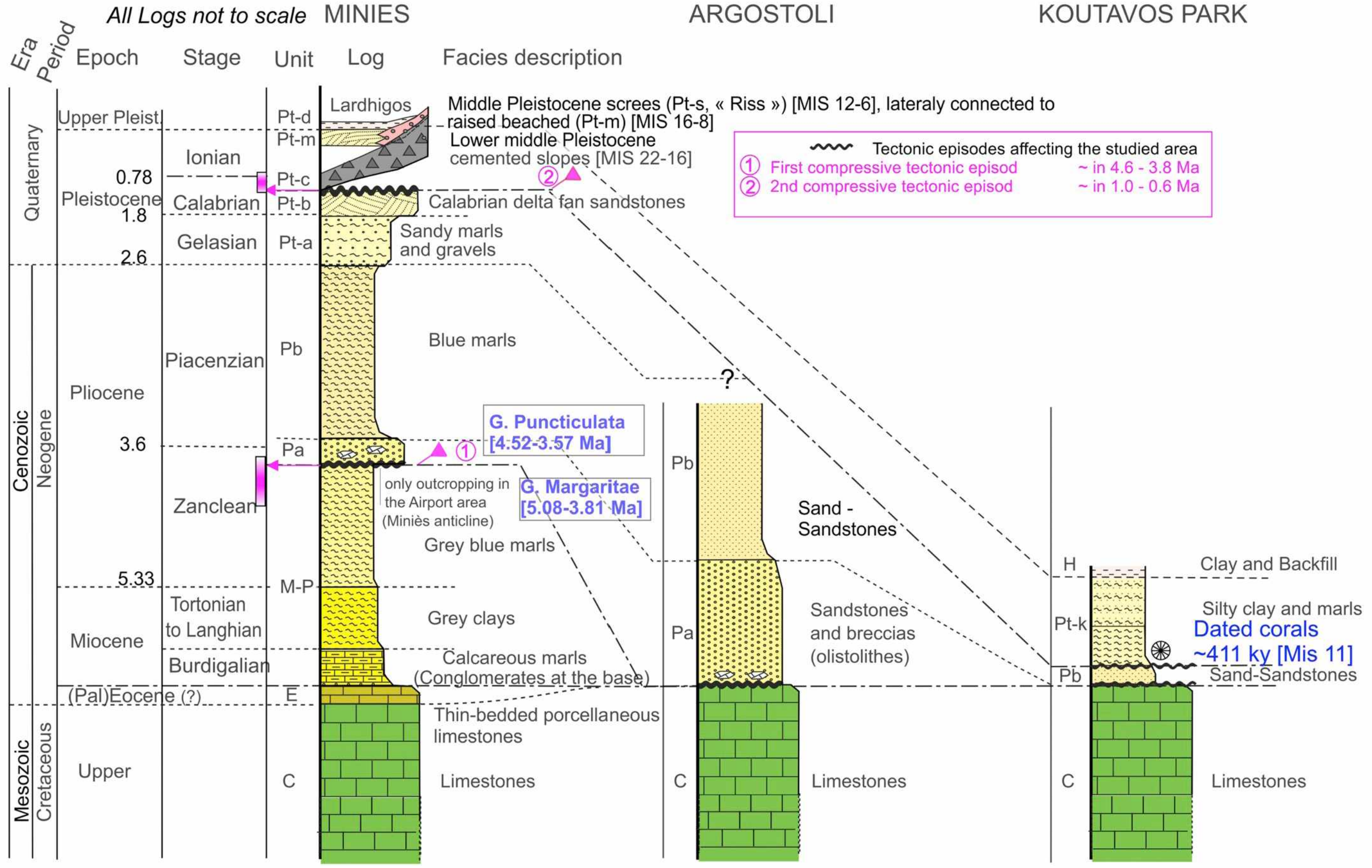

Fig. 9. Minies, Argostoli, and Koutavos lithostratigraphic logs (not to scale). Geological ages are provided to the left of each log, along with the nomenclature adopted throughout the text.

agreement between HVSR typologies and geologic limits (e.g. double-peak typologies located near the outcropping limit between the *Pa* and the *Pt-k* units or the transition between Type 1 and Type B typologies as the signature between *Pa*and *Pb*units) gives a good confidence about these limits.

Then, we constructed four geological cross-sections (Fig. 11), to highlight the 2D variations of the lithostratigraphic units above the bedrock (i.e., the Upper Cretaceous unit), from the Eocene unit to the Middle Pleistocene and Quaternary units. Three geological cross-sections were constructed perpendicular to the axis of the depocenter of the present-day Argostoli basin. An additional geological cross-section was constructed by cutting perpendicularly the three previous cross-sections, approximately above the main depocenter of the basin.

All of the geological cross-sections were constrained by the lithostratigraphic limits of the updated geological map (Fig. 10), the dip measurements, and the depths of the lithostratigraphic limits interpreted from some of the 17 water borehole logs that were available in the Argostoli area. However, all of these water boreholes are not reliable because their loggings were not done for geological purpose. Only those having stratigraphic limits coherent with the local geology knowledge based on field observation were taken into account. Complementary boreholes located near the De Bosset Bridge were also used (Rovithis et al., 2014). Additional depths of the lithostratigraphic limits were obtained by the joint interpretation of f_0 values provided by HVSR and velocity profiles provided by SWDA allowing converting f_0 into depth of velocity contrasts. These cross-sections are described in the following:

i. ***Cross-section PR01:*** This cross-section is 5.3 km long and crosses through the Argostoli basin with a SW-NE orientation (see Figs. 5 and 9). PR01 cuts through the Plio-Calabrian syncline located west of Lardhigos Cape, Saint Gerasismos Cave, the Airport road, and the main road of Argostoli. It comprises the Argostoli anticline and the Argostoli basin, faulted by the reverse White-Rock Fault; Minies Fault and Argostoli Fault. In the Koutavos area, PR01 is constrained by the borehole BK0. In the Argostoli basin, the depth of the Upper Cretaceous bedrock ranges from 100 m a.s.l. (above sea level) to 200 m b.s.l. (below sea level).
ii. ***Cross-section PR02:*** This cross-section is 5 km long and is oriented SW-NE. It crosses through the Argostoli basin with a SW-NE orientation (see Figs. 5 and 9). PR02 cuts through the Airport road and the main road of Argostoli. PR02 is constrained by four boreholes near Koutavos Park: B17, B20, B13 and B09. Along this cross-section, the depth of the Upper Cretaceous bedrock is around 50 m b.s.l. east of the main road, in the axis prolongation of Koutavos Park, and nearly 120 m b.s.l. west of the main road, and south of the city of Argostoli.
iii. ***Cross-section PR03:*** This cross-section is oriented SW-NE and is located in the southern part of the Argostoli basin. It is 6.5 km long, and crosses through the Argostoli basin with a SW-NE orientation (see Figs. 5 and 9). PR03 also cuts through the Airport road and the main road of Argostoli. Along PR03 there are five water boreholes: B06, B11, B08, B04 and B10. Only B06, B11 and B10 are coherent with observed local geology and are, thus, drawn on Fig. 11. In this part of the Argostoli basin, the depth of the Upper Cretaceous bedrock reaches 90 m b.s.l.
iv. ***Cross-section PR04***: This cross-section is oriented NW-SE and follows the axis of the Argostoli basin passing through its depocenter. It is 4.5 km long, and it crosses the entire Argostoli basin (see Figs. 5 and 9), from the Koutavos Park area to the southeastern part of the

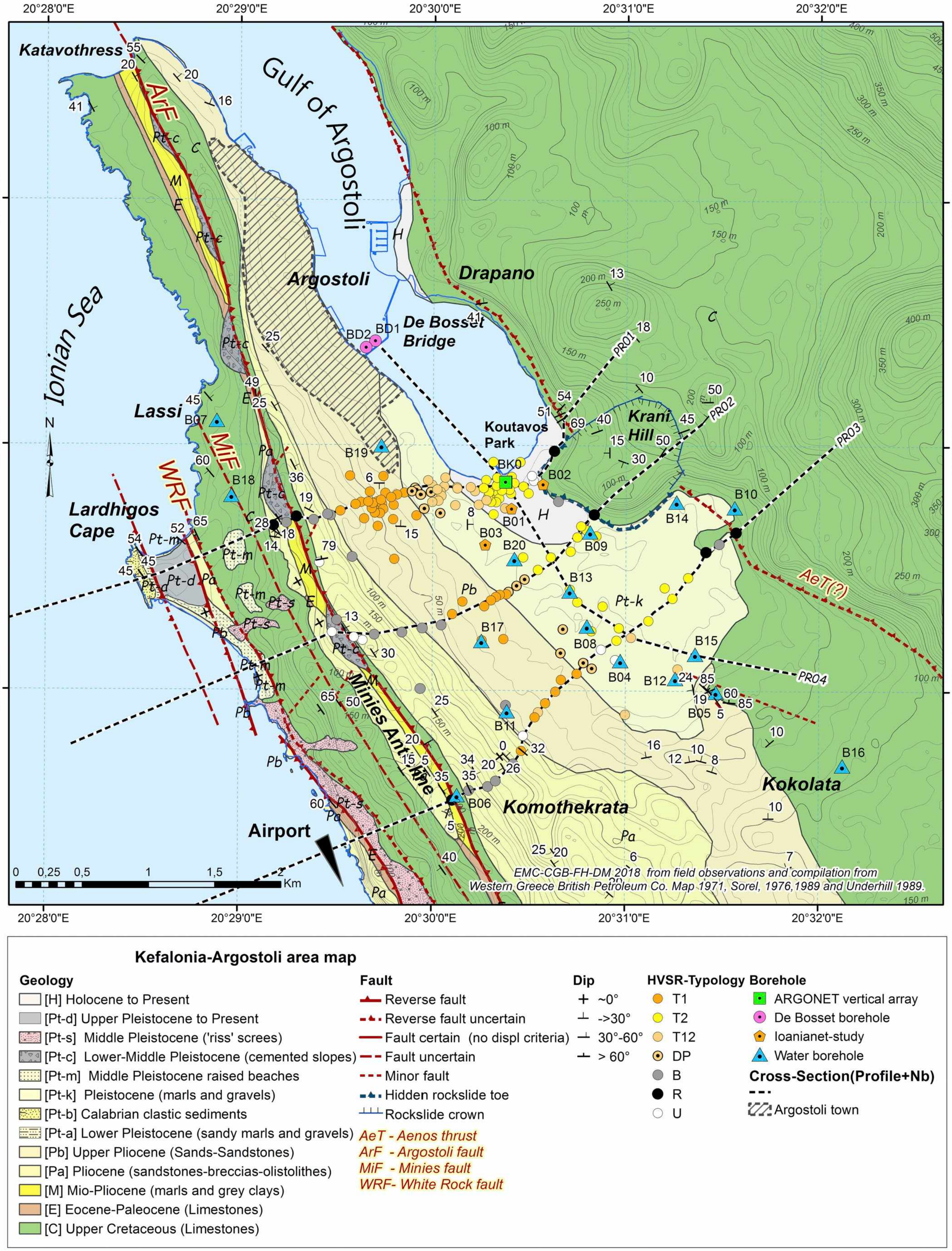

Fig. 10. Updated geological map of the Argostoli area with the spatial distribution of the HVSR typology (explained in the text, Section 3.2) and the locations of boreholes and geological and geophysical surveys (either pre-existing or conducted within the frame of this work).

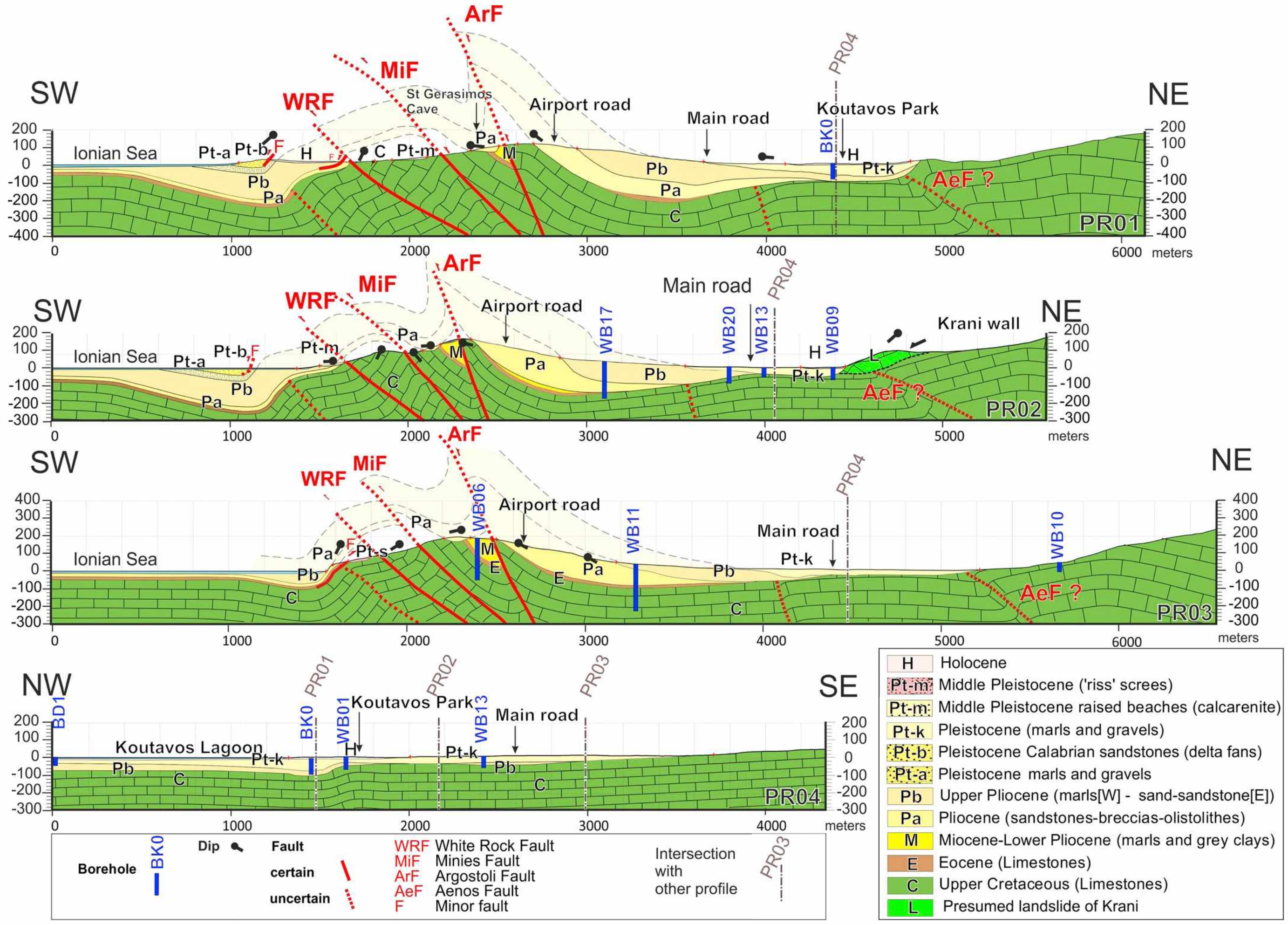

Fig. 11. Geological cross-sections of the Argostoli basin.

basin. PR04 is constrained by the three previous cross-sections, PR01, PR02, and PR03, and by some boreholes: two in Koutavos Park (BK0, WB01), and the WB13 south of Koutavos Park. Along this profile, the depth of the Upper Cretaceous bedrock ranges from 20 m a.s.l. to 90 m b.s.l.

The construction of these four cross-sections based on the geological survey and geophysical interpretation leads to an image of the three sets of Plio-Pleistocene layers that become thinner moving away from the hanging wall of the Argostoli-Minies reverse fault. This geometry can be interpreted as the result of the eastward displacement of the depocenter due to a continuous process of deposition along the growing anticline. This can also be explained by lateral variation of the facies across the Argostoli Gulf, as was proposed by Sorel (1989, 1976). Consideration of the dating of the coral debris sustains the continuous activity of the Argostoli syncline hypothesis (see Section 2.2). The retro-deformation sketch proposed in Fig. 12 provides an understanding of the structural relationships between each sedimentary set: first, an extensional period occurred from the Miocene to Lower Pliocene. That was characterized by normal faulting that affecting the Pre-Apulian series. In the lower Pliocene, a first shortening provoked the inversion along the previous normal faults. This period coincided with the inclusion of the Pre-Apulian continental crust in the Aegean Arc. This period ended with an erosion phase associated with marine transgression. From Middle Pliocene to Lower Quaternary, a quiet period with subsidence and detrital deposits ended with the Calabrian regression. A Second and strong inversion enhanced the folded structure and faults.

4.3. Three-dimensional geological model of the Argostoli basin

All of the available geological and geophysical data were compiled using the Geographic Information System software ArcGis 10.2.1 for Desktop (ESRI). This data was used as constraints for the surface interpolation which was performed using the Tool 'Topo to Raster' coming with the Spatial Analyst extension of ArcGis GIS and using the default parameters. Input control points used come from: (1) borehole interpretation, cross-sections (spatially referenced interface points extracted from line-drawings); (2) digitized points with altimetry information of the geological map contours of each unit; and (3) estimated depths deduced from the HVSR surveys and the complementary f_0 values from the SWDA f_0 arrays measurements. These control points are represented as dots on the maps in Fig. 13. The Basin model is focused on the Argostoli Basin located on the eastern rim of The Argostoli Anticline. Thus, the Mio-Pliocene interface west of the Argostoli Fault has not been taken in account and the so called 'Top of the Cretaceous surface' is actually only the topographic surface on the western flank of the Argostoli anticline.

Fig. 13 presents the 3D geological model of the Argostoli basin, showing the depth geometry and spatial distribution of the three lithostratigraphic interfaces as the top of the Cretaceous unit, the base of the *Pb* unit, and the base of the *Pt-k* unit (Fig. 13a). The raster has 10 m × 10 m resolution, and the pixel value represents the altitude above (or below – as negative values when the interface is below mean sea level). From the above-mentioned raster, three more raster datasets were constructed by determining the arithmetic differences between

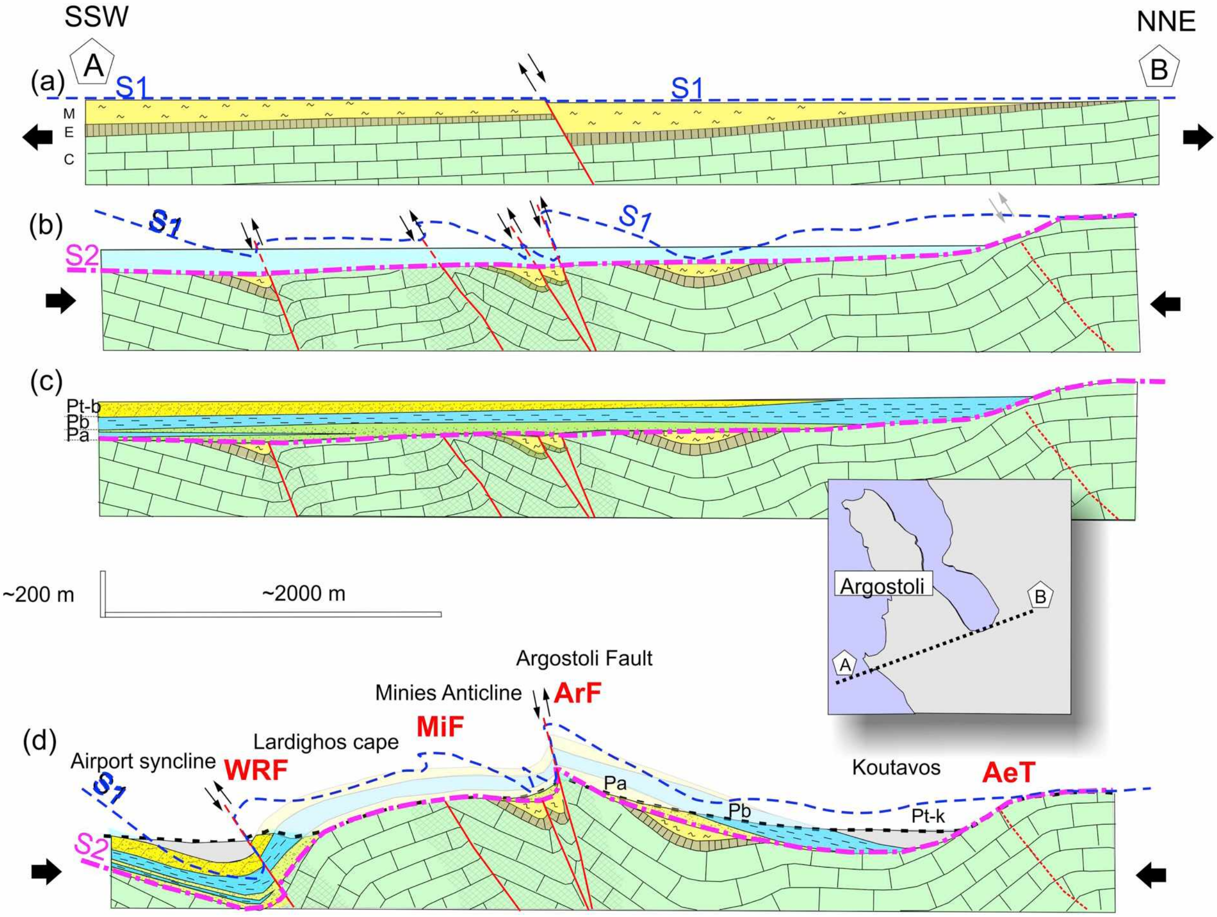

Fig. 12. Retro-tectonic sketch of the Argostoli anticline/ syncline since the Extensional period (Miocene to Lower Pliocene). (a) Normal faulting that affected the Pre-Apulian series. (b) First shortening that provoked inversion along the previous normal faults. This period coincided with the inclusion of the Pre-Apulian continental crust in the Aegean Arc. This period ended with an erosion phase associated with marine transgression – following stage (c) From Middle Pliocene to Lower Quaternary, quiet period with subsidence and detrital deposits that ended with the Calabrian regression (delta fans). (d) Second and strong inversion that enhanced the folded structure and faults. This sketch is an adaptation of those from Sorel (1989) and Underhill (1989). Reference surfaces S1 and S2 correspond to the end of the sedimentation (Lower Pliocene), and to the Lower-Middle Pliocene erosional surface, respectively. Hatched areas illustrate the dolomitized and strongly brecciated areas along the main faults (i.e., Argostoli, Minies, White Rock). The inset shows the position of the cross section A-B which is close to the HVSR profile 01(Figs. 5 and 10).

the previous datasets, to obtain the thickness image of each unit (i.e., Fig. 13b, thicknesses of *Pa, Pb, H* + *Pt-k*). A 3D sketch of the three interfaces is presented in Fig. 13c.

In this model, the top of the Cretaceous bedrock forms the base surface and controls the sharp variations in the thickness of the Pleistocene sedimentary cover (Fig. 13a). The surface reveals an incised valley, with a steep slope on the western flank, and a more progressive slope on the eastern flank, which highlights the asymmetrical shape of the valley. The elevation of the top Cretaceous surface ranges from −180 m to −200 m with respect to sea level (w.r.s.l.), from the deepest part of the surface, south of the city of Argostoli, to the western flank of the basin, close to the Airport road. The thickness map of the *Pa*unit (Fig. 13a, left) highlights the spatial distribution of the Lower Pliocene *Pa*unit deposits above the Cretaceous bedrock. The Argostoli basin has a *Pa*unit thickness that ranges from 0 m to 190 m. The main depocenter line strikes NNW-SSE, and is located close to the western flank of the valley, along the present-day Airport road. This map shows that the *Pa*sediments are located throughout the entire Argostoli basin, and are bounded to the south by a structural high, of the Upper Cretaceous age. To the north, the interpolation has been cut due to a lack of data.

Fig. 13a (middle) shows the present-day altitude of the base surface of the *Pb*unit, of the Pliocene (Piacenzian) age. The surface morphology of the *Pb*unit reveals an incised valley, with both eastern and western flanks showing progressive slope, which highlights the symmetrical shape of the valley at this step in the history of the basin. The altitude of the surface base of the *Pb*unit ranges from −100 m to −120 m w.r.s.l., from the deepest part of the surface, south of the city of Argostoli to the south of the basin, close to the village of Kokolata (see Fig. 2). The deepest zone (Fig. 13a, middle, in blue color) is about −80 w.r.s.l. on average. The thickness map of the *Pb*unit in Fig. 13b (middle) highlights the spatial distribution of the Pliocene *Pb*unit deposits above the *Pa*unit deposits. The main depot center line strikes NNW-SSE, and is located close to the western flank of the valley, as for the *Pa*unit. The maps in Fig. 13 also show that the *Pb*sediments are located in the entire Argostoli basin, and that they disappear to the south. There are no *Pb*deposits in the southeastern part of the Koutavos area. To the north, the interpolation has been cut due to a lack of data.

The variations in the thickness of the *Pt-k* unit show a narrow valley with a steep slope on the eastern flank and a more progressive slope on the western flank. The altitude of the base surface of the *Pt-k* unit ranges from −80 m to −40 m w.r.s.l. The *Pt-k* sediments body strikes NNW-SSE, and is located close to the eastern flank of the valley. These maps show that the *Pt-k* sediments are mainly located around two main depocenters (Fig. 13).

It needs to be kept in mind that the resolution of these maps remains coarse for altimetric positions of interfaces and for thicknesses with regard to the numerous interpretations and interpolations carried out. However, this first dataset could be useful for further computation of

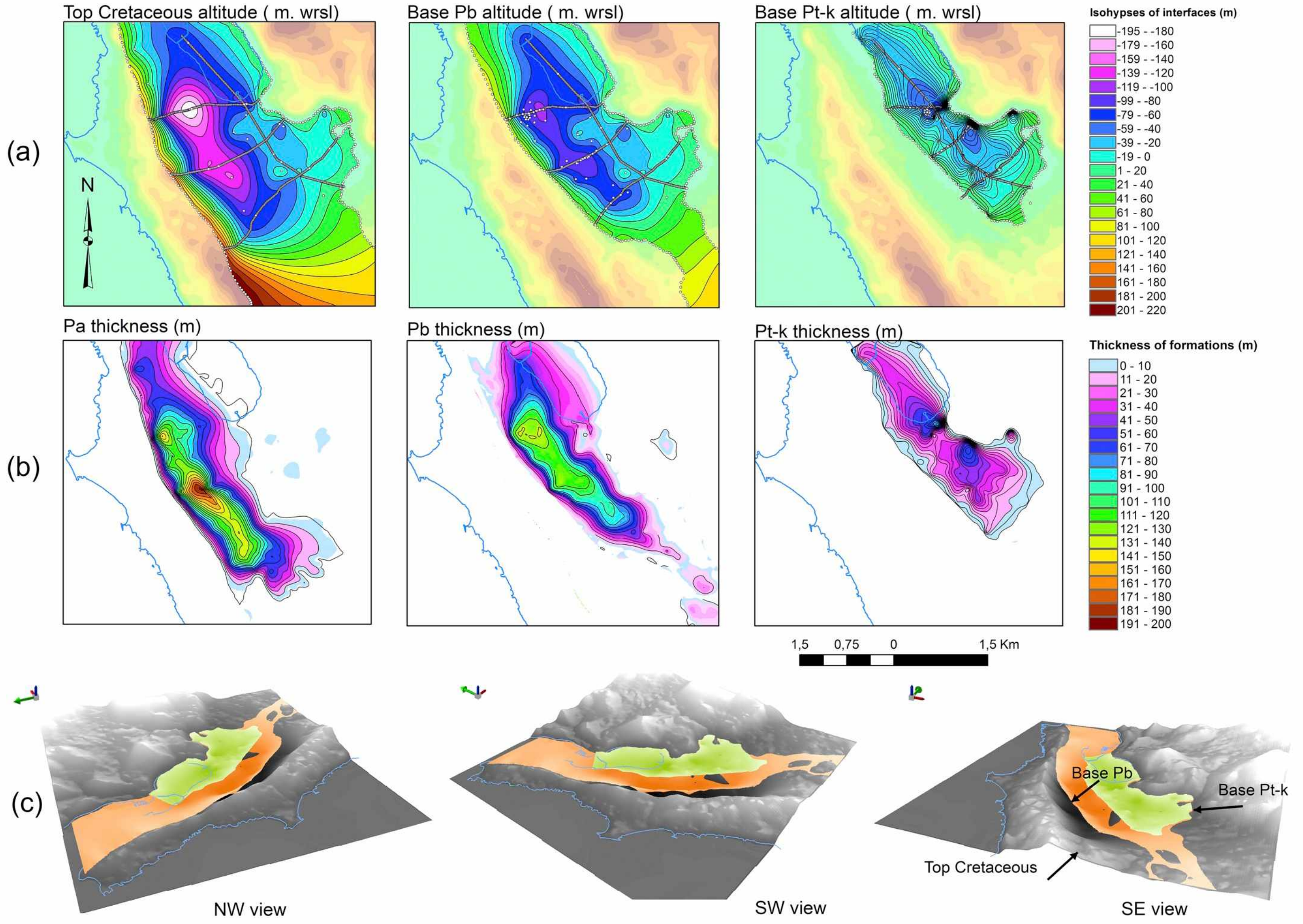

Fig. 13. Three-dimensional model of the Argostoli Plio-Quaternary basin. (a) Isohypses with respect to the sea level of the three interfaces: top of the Cretaceous limestone; base of *Pb* (Piacenzian); and *Pt-k* (Middle Pleistocene of the Koutavos area). Control points (mapped outcrops, line drawing of interfaces on cross-sections and inferred depths from HVSR analysis) are also shown. (b) Thicknesses (in m) deduced from isohypses geometry (*Pa, Pb, Pt-k* thickness). (c) Three-dimensional representation of the three interfaces from different azimuths.

3D site effects (Touhami et al., 2019). Moreover, this mapping and the cross-sections and geophysical and borehole data will be useful for further studies of the effects of complex surface geology on ground motion.

5. Conclusions

To facilitate studies on site-specific amplification and non-linear behavior of soil in the framework of seismic hazard assessment for nuclear infrastructure installation, the Koutavos site in Cephalonia was chosen as a test site to validate 3D simulation algorithms. The selection of the site was done considering both the geological structure as well as the high seismicity rate of the area based on various geo-information. The aim of this present study specifically, was to improve the overall geological knowledge of the area and to build a 3D structural model of the Plio-Quaternary basin of the Argostoli-Koutavos area.

1) Several geological investigations and geophysical measurements were performed in the study area. Dating performed on coral debris coming from the Koutavos Borehole confirms the Pleistocene age of the Koutavos basin.
2) The geophysical surveys involved single-station ambient vibration measurements for horizontal-to-vertical spectral ratio analyses (HVSR) as well as passive ambient vibration array (AVA) complemented by active MASW measurements for surface wave dispersion analysis (SWDA). The analysis of the HVSRs led to the identification of several HVSR curve typologies. The HVSR measurements confirmed that the most likely and geologically consistent interpretation includes the presence of a single basin. Complementary to these data, six areas were investigated by SWDA, to measure the V_S in the bedrock and along a cross-section perpendicular to the basin axis. Three reference velocity models were finally proposed one for the bedrock (Cretaceous limestone and Pliocene sandstone and breccias) one for the Pliocene (sands and sandstone formations) and one for the Pleistocene/Holocene (soft clays and sands, lagoonal sediments layer).
3) Four geological cross-sections were constructed considering each fundamental resonance frequency (f_0) value on profiles and the velocity contrasts previously defined. These data were used as constraints for surfaces interpolation and finally to build the 3D geological model.

The methodology proposed in this work could be applied to similar basin environments not only of high but of moderate-to-low seismicity areas worldwide, considering and adopting local peculiarities. It is well known that in earthquake engineering all geological and geophysical parameters estimated in this study play a fundamental role in the generation and propagation of the seismic waves since local ground motion amplification is primarily controlled by geometric complexities in the bedrock morphology and seismic velocity contrasts of sedimentary layers.

The results of this study can be considered as the first step toward a scenario-based seismic hazard analysis and its associated risk for population and infrastructure. In fact, the lessons to be learnt from 3D seismic wave modeling by computing ground motion intensity measures (PGA, PGV, Response Spectral Values, Duration etc.) will be extremely useful for engineering purposes. Such usefulness will not be restricted to the specific investigated basin but would be extended to similar cases through proper correlation of basin geological/geophysical factors with calculated intensity measures for various earthquake scenarios. Furthermore, such studies followed by proper simplification could in turn contribute to seismic code provisions toward risk mitigation.

Finally, the location of the investigated Argostoli basin is of high earthquake engineering importance, being a near-fault zone (CTFZ) ‘laboratory’ subjected in the recent past to significant tectonic movements and near-field high level ground motion intensity, with a potential to excite ground motion non-linearity and liquefaction phenomena. The seismic instrumentation deployed during the last ten years in the basin and its vicinity (NERA and SINAPS@ projects) as well as the existing and continuously operating since 2015 ARGONET vertical array, are providing high quality data. Due to limited worldwide of similar near-fault seismic observatories the contribution of this study to earthquake engineering and risk reduction becomes indisputable.

Acknowledgments

This project was conceived after the NERA-JRA1 and SIGMA/PRENOLIN projects, and then funded by the French National Agency for Research (ANR) in the framework of the program *Investissements d'avenir* (PIA): SINAPS@ (ANR-11-RSNR-0022; www.institut-seism.fr/en/). The local authorities warmly welcomed the project and helped to obtain all of the necessary authorizations. Our thanks also go to Agis Konidaris, Chrisostomos Andreou, Geoter Co., and the Geophysical Laboratory of Thessaloniki. The authors also thank Olivier Dufaure and Serge Miska from GEOPS for their technical assistance in the X-ray diffraction sample preparation and analysis, and the team participants for the field measurements, Elise Delavaud, Myrtille Kuperminc, Vincent Perron, and Sara Touhami and Michael Darche. The comments by the Editor, Dr. Wasowski, and by two anonymous reviewers were helpful to improve our manuscript. We finally thank Chris Berrie for helping us to perform the English wording of the paper.

Declaration of Competing Interest

The authors declare that they have no known competing financial interests or personal relationships that could have appeared to influence the work reported in this paper.

Appendix A

Table A.1

Measured points of HVSR (HVSR profile measures, AVA measures and few complementary points). This list is ordered by profile or network. Locations (geographic – WGS), Resonance frequencies interpretation and Peak typology are reported as explained in the text.

No.	Dataset	Point name	Latitude (decimal)	Longitude (decimal)	f0/f1 (Hz)	fo (when DP –Hz)	Typology (see text)	Large amp
1	Profile 1	PR01-01	38.161188	20.486319	0.73		R	
2	Profile 1	PR01-02	38.161369	20.487433	7.64		B	
3	Profile 1	PR01-03	38.161789	20.488303	7.42		R	
4	Profile 1	PR01-04	38.161573	20.489775	3.29		B	
5	Profile 1	PR01-05	38.161956	20.490981	3.39		B	
6	Profile 1	PR01-06	38.162184	20.492074	3.19		T1	
7	Profile 1	PR01-07	38.162632	20.493389	1.46		T1	
8	Profile 1	PR01-08	38.162813	20.494470	1.50		T1	
9	Profile 1	PR01-09	38.162929	20.495578	1.50		T1	
10	Profile 1	PR01-10	38.163118	20.496449	1.50		T1	
11	Profile 1	PR01-11	38.163295	20.496953	1.46		T1	
12	Profile 1	PR01-12	38.163431	20.497588	1.46		T1	
13	Profile 1	PR01-13	38.163522	20.498246	50.00	1.65	DP	
14	Profile 1	PR01-14	38.163625	20.498651	15.74	1.65	DP	
15	Profile 1	PR01-15	38.163958	20.499951	4.31		T12	
16	Profile 1	PR01-16	38.163865	20.500995	3.19		T12	
17	Profile 1	PR01-17	38.163810	20.502100	2.36		T12	
18	Profile 1	PR01-18	38.163820	20.503270	2.22		T12	
19	Profile 1	PR01-19	38.163750	20.504390	2.09		T2	
20	Profile 1	PR01-20	38.164000	20.505550	1.60		T2	
21	Profile 1	PR01-21	38.163991	20.506523	1.65		T2	
22	Profile 1	PR01-22	38.163870	20.507820	1.75		T2	
23	Profile 1	PR01-23	38.164260	20.508710	3.29		U	
24	Profile 1	PR01-24	38.162860	20.510840	9.43		B	
25	Profile 2	PR02-01	38.153938	20.491407	3.29		U	
26	Profile 2	PR02-02	38.153601	20.493293	5.49		U	
27	Profile 2	PR02-03	38.153392	20.494038	4.72		U	
28	Profile 2	PR02-04	38.153783	20.495050	5.01		B	
29	Profile 2	PR02-06	38.153936	20.497436	2.43		B	
30	Profile 2	PR02-07	38.154225	20.499172	2.51		B	
31	Profile 2	PR02-08	38.154432	20.500779	5.65		B	
32	Profile 2	PR02-09	38.155182	20.501718	1.42		T1	
33	Profile 2	PR02-10	38.156032	20.502604	1.65		T1	
34	Profile 2	PR02-11	38.155716	20.504487	1.65		T1	
35	Profile 2	PR02-12	38.156128	20.505057	1.60		T1	
36	Profile 2	PR02-13	38.156353	20.505483	1.70		T1	
37	Profile 2	PR02-14	38.156496	20.505824	1.70		T1	
38	Profile 2	PR02-15	38.156546	20.506375	1.80		T1	
39	Profile 2	PR02-16	38.156703	20.506569	6.01	1.80	DP	
40	Profile 2	PR02-17	38.157121	20.507267	4.72	2.20	DP	

(*continued on next page*)

Table A.1 (*continued*)

No.	Dataset	Point name	Latitude (decimal)	Longitude (decimal)	f0/f1 (Hz)	fo (when DP –Hz)	Typology (see text)	Large amp
41	Profile 2	PR02-18	38.157551	20.507946	4.72	2.20	DP	
42	Profile 2	PR02-19	38.158210	20.509103	3.94		T2	
43	Profile 2	PR02-20	38.159055	20.510209	2.36		T2	
44	Profile 2	PR02-21	38.159468	20.511914	1.80		T2	
45	Profile 2	PR02-22	38.160438	20.512485	1.75		T2	
46	Profile 2	PR02-23	38.161182	20.512818	1.80		T2	
47	Profile 2	PR02-24	38.161971	20.513945	19.43		R	
48	Profile 3	PR03-01	38.142526	20.501780	0.51		R	
49	Profile 3	PR03-02	38.143191	20.503225	2.66		B	
50	Profile 3	PR03-03	38.143461	20.504855	3.39		B	
51	Profile 3	PR03-04	38.143840	20.505522	3.49		B	
52	Profile 3	PR03-05	38.145017	20.507025	2.16		B	
53	Profile 3	PR03-06	38.145898	20.507716	6.57		T1	
54	Profile 3	PR03-07	38.146925	20.507871	19.43		U	
55	Profile 3	PR03-08	38.148185	20.508870	5.65		T1	
56	Profile 3	PR03-09	38.149148	20.509780	2.43		T1	
57	Profile 3	PR03-10	38.149934	20.510645	2.16		T1	
58	Profile 3	PR03-11	38.150736	20.511127	2.22		T1	
59	Profile 3	PR03-12	38.151152	20.512480	2.36		T1	
60	Profile 3	PR03-13	38.151515	20.513775	12.00	2.43	DP	
61	Profile 3	PR03-14	38.152806	20.514567	2.43		U	
62	Profile 3	PR03-15	38.153417	20.515893	3.00		T2	
63	Profile 3	PR03-17	38.153616	20.517143	3.19		T12	
64	Profile 3	PR03-19	38.154766	20.518646	3.49		T2	
65	Profile 3	PR03-21	38.156283	20.520709	3.71		T2	
66	Profile 3	PR03-22	38.157701	20.522057	3.82		T2	
67	Profile 3	PR03-24	38.159451	20.523579	9.15		R	
68	Profile 3	PR03-25	38.159989	20.524723	16.72		B	
69	Profile 3	PR03-26	38.160776	20.526187	13.14		R	
70	Large Array	A3-R0	38.154053	20.513725	3.49		T2	
71	Large Array	A3-R230-1	38.155739	20.514696	2.09		T2	
72	Large Array	A3-R230-2	38.154266	20.516102	2.66		T2	
73	Large Array	A3-R230-3	38.152103	20.515784	2.66		U	
74	Large Array	A3-R230-4	38.151894	20.513042	12.00	2.22	DP	
75	Large Array	A3-R230-5	38.152559	20.511074	14.38	2.22	DP	
76	Large Array	A3-R230-6	38.154180	20.511267	12.00	5.01	DP	
77	Large Array	A3-R230-7	38.156022	20.512504	2.29		T2	
78	Large Array	A3-R700-1	38.160505	20.514133	1.75		T2	
79	Large Array	A3-R700-2	38.157003	20.520029	2.59		T2	
80	Large Array	A3-R700-3	38.151487	20.521176	8.12		T12	
81	Large Array	A3-R700-4	38.148391	20.516662	4.18		T12	
82	Large Array	A3-R700-5	38.148530	20.509165	3.82		T12	
83	Large Array	A3-R700-6	38.153493	20.506140	1.91		T1	
84	Large Array	A3-R700-7	38.159057	20.507816	3.60		T2	
85	Array 2	A2-R0	38.162361	20.495200	1.50		T1	
86	Array 2	A2-R135-1	38.163405	20.495952	1.50		T1	
87	Array 2	A2-R135-2	38.162593	20.496671	1.55		T1	
88	Array 2	A2-R135-3	38.161612	20.496627	1.50		T1	
89	Array 2	A2-R135-4	38.161145	20.495314	1.55		T1	
90	Array 2	A2-R135-5	38.161662	20.494129	1.50		T1	
91	Array 2	A2-R135-6	38.162782	20.493857	1.50		T1	
92	Array 2	A2-R135-7	38.163483	20.494613	1.50		T1	
93	Array 2	A2-R45-1	38.162825	20.495280	1.55		T1	
94	Array 2	A2-R45-2	38.162663	20.495681	1.50		T1	
95	Array 2	A2-R45-3	38.162306	20.495776	1.50		T1	
96	Array 2	A2-R45-4	38.162032	20.495493	1.50		T1	
97	Array 2	A2-R45-5	38.162056	20.495045	1.50		T1	
98	Array 2	A2-R45-6	38.162365	20.494777	1.50		T1	
99	Array 2	A2-R45-7	38.162721	20.494879	1.55		T1	
100	Array 2	A2-RL-1	38.164540	20.495779	1.55		T1	
101	Array 2	A2-RL-2	38.163758	20.498505	8.88	1.80	DP	
102	Array 2	A2-RL-3	38.161879	20.498639	1.60		T1	
103	Array 2	A2-RL-4	38.158911	20.496749	1.80		T1	
104	Array 2	A2-RL-5	38.159059	20.493118	7.64		B	
105	Array 2	A2-RL-6	38.161878	20.491230	3.60		B	
106	Array 2	A2-RL-7	38.164570	20.492900	2.03		T1	
107	Array 3	WEST_R0_A0	38.163252	20.500263	4.27		T12	
108	Array 3	WEST_R3_A1	38.163649	20.500385	4.16		T12	
109	Array 3	WEST_R3_A2	38.163492	20.500667	3.95		T12	
110	Array 3	WEST_R3_A3	38.163224	20.500740	3.84		T12	
111	Array 3	WEST_R3_A4	38.162887	20.500486	4.63		T12	
112	Array 3	WEST_R3_A5	38.162797	20.499959	5.73		T12	
113	Array 3	WEST_R3_A7	38.163480	20.499840	5.01	1.68	DP	
114	Array 3	WEST_R4_A1	38.164458	20.501089	2.32		T12	

(*continued on next page*)

Table A.1 (*continued*)

No.	Dataset	Point name	Latitude (decimal)	Longitude (decimal)	f0/f1 (Hz)	fo (when DP –Hz)	Typology (see text)	Large amp
115	Array 3	WEST_R4_A2	38.163725	20.502127	2.26		T12	
116	Array 3	WEST_R4_A3	38.162580	20.501949	3.45		T12	
117	Array 3	WEST_R4_A4	38.162046	20.500657	5.80	1.60	DP	
118	Array 3	WEST_R4_A5	38.162346	20.499276	28.30	1.60	DP	
119	Array 3	WEST_R4_A6	38.163302	20.498989	12.40	1.60	DP	
120	Array 3	WEST_R4_A7	38.164270	20.499594	4.39		T12	
121	Array 4	A1-R0	38.163149	20.505247	1.65		T2	
122	Array 4	A1-R135-1	38.164242	20.505910	1.50		T2	1
123	Array 4	A1-R135-2	38.163387	20.506747	1.75		T2	
124	Array 4	A1-R135-3	38.162380	20.506240	1.70		U	
125	Array 4	A1-R135-4	38.161973	20.505257	2.22		T2	
126	Array 4	A1-R135-5	38.162624	20.503974	3.29		T12	
127	Array 4	A1-R135-6	38.163548	20.503634	2.16		T12	
128	Array 4	A1-R135-7	38.164304	20.504606	1.60		T2	
129	Array 4	A1-R45-1	38.163572	20.505237	1.60		T2	1
130	Array 4	A1-R45-2	38.163406	20.505670	1.60		T2	1
131	Array 4	A1-R45-3	38.163050	20.505728	1.60		T2	
132	Array 4	A1-R45-4	38.162798	20.505469	1.91		T2	
133	Array 4	A1-R45-5	38.162819	20.505039	1.70		T2	
134	Array 4	A1-R45-6	38.163123	20.504760	1.70		T2	
135	Array 4	A1-R45-7	38.163467	20.504842	1.65		T2	
136	Array 5	ARGO_R0_A0	38.164180	20.506234	1.60		T2	1
137	Array 5	ARGO_R4_A1	38.164533	20.506795	1.43		T2	1
138	Array 5	ARGO_R4_A2	38.164104	20.507036	1.40		T2	1
139	Array 5	ARGO_R4_A3	38.163652	20.506618	1.68		T2	
140	Array 5	ARGO_R4_A4	38.163595	20.505955	1.60		T2	
141	Array 5	ARGO_R4_A5	38.163925	20.505508	1.60		T2	
142	Array 5	ARGO_R4_A6	38.164458	20.505551	1.55		T2	1
143	Array 5	ARGO_R5_A1	38.165535	20.507547	1.43		T2	1
144	Array 5	ARGO_R5_A2	38.164590	20.508549	2.58		U	
145	Array 5	ARGO_R5_A3	38.163406	20.508262	1.82		T2	
146	Array 5	ARGO_R5_A4	38.162392	20.506239	1.73		T12	
147	Array 5	ARGO_R5_A5	38.162930	20.504644	2.26		T12	
148	Array 5	ARGO_R5_A7	38.165538	20.505211	1.43		T2	1
149	Compl. Point	CP-01	38.156866	20.511862	2.36		T2	
150	Compl. Point	CP-02	38.158679	20.490289	8.12		U	
151	Compl. Point	CP-03	38.154764	20.491797	19.43		B	
152	Compl. Point	CP-05	38.160919	20.513277	2.22		T2	
153	Compl. Point	CP-06	38.166288	20.510489	6.98		R	
154	Compl. Point	CP-07	38.153404	20.504282	2.09		T1	
155	Compl. Point	CP-08	38.148995	20.506361	5.49		B	
156	Compl. Point	CP-09	38.150107	20.499009	3.49		B	

Appendix B. Supplementary data

Supplementary data associated with this article can be found in the online version, at doi:https://doi.org/10.1016/j.enggeo.2019.105441. These data include the Google map of the most important areas described in this article.

References

Akyol, N., Kurtulmuş, T., Çamyildiz, M., Güngör, T., 2013. Spectral ratio estimates for site effects on the Horst-Graben System in West Turkey. Pure Appl. Geophys. 170, 2107–2125. https://doi.org/10.1007/s00024-013-0661-2.

Andersen, M.B., Stirling, C.H., Potter, E.-K., Halliday, A.N., Blake, S.G., McCulloch, M.T., Ayling, B.F., O'Leary, M., 2008. High-precision U-series measurements of more than 500,000 year old fossil corals. Earth Planet. Sci. Lett. 265, 229–245. https://doi.org/10.1016/j.epsl.2007.10.010.

Aubouin, J., 1959. Contribution à l'étude de la Grèce septentrionale : les confins de l'Épire et de la Thessalie. Ann. Géologiques Pays Hell. X 483.

Aubouin, J., Dercourt, J., 1962. Zone préapulienne, zone ionienne et zone du Gavrovo en Péloponnèse occidental. Bull. Société Géologique Fr. 7, 785–794.

Avallone, A., Cirella, A., Cheloni, D., Tolomei, C., Theodoulidis, N., Piatanesi, A., Briole, P., Ganas, A., 2017. Near-source high-rate GPS, strong motion and InSAR observations to image the 2015 Lefkada (Greece) Earthquake rupture history. Sci. Rep. 7, 10358. https://doi.org/10.1038/s41598-017-10431-w.

Bard, P.-Y., Cadet, H., Endrun, B., Hobiger, M., Renalier, F., Theodulidis, N., Ohrnberger, M., Fäh, D., Sabetta, F., Teves-Costa, P., Duval, A.-M., Cornou, C., Guillier, B., Wathelet, M., Savvaidis, A., Köhler, A., Burjanek, J., Poggi, V., Gassner-Stamm, G., Havenith, H.B., Hailemikael, S., Almeida, J., Rodrigues, I., Veludo, I., Lacave, C., Thomassin, S., Kristekova, M., 2010. From non-invasive site characterization to site amplification: Recent advances in the use of ambient vibration measurements. In: Garevski, M., Ansal, A. (Eds.), Earthquake Engineering in Europe. Springer, Netherlands, Dordrecht, pp. 105–123. https://doi.org/10.1007/978-90-481-9544-2_5.

Basili, R., Kastelic, V., Demircioglu, M.B., Garcia Moreno, D., Nemser, E.S., Petricca, P., Sboras, S.P., Besana-Ostman, G.M., Cabral, J., Camelbeeck, T., Caputo, R., Danciu, L., Domac, H., Fonseca, J., García-Mayordomo, J., Giardini, D., Glavatovic, B., Gulen, L., Ince, Y., Pavlides, S., Sesetyan, K., Tarabusi, G., Tiberti, M.M., Utkucu, M., Valensise, G., Vanneste, K., Vilanova, S., Wössner, J., 2013. The European Database of Seismogenic Faults (EDSF) Compiled in the Framework of the Project SHARE. https://doi.org/10.6092/INGV.IT-SHARE-EDSF.

Berge-Thierry, C., Svay, A., Laurendeau, A., Chartier, T., Perron, V., Guyonnet-Benaize, C., Kishta, E., Cottereau, R., Lopez-Caballero, F., Hollender, F., Richard, B., Ragueneau, F., Voldoire, F., Banci, F., Zentner, I., Moussallam, N., Lancieri, M., Bard, P.-Y., Grange, S., Erlicher, S., Kotronis, P., Le Maoult, A., Nicolas, M., Régnier, J., Bonilla, F., Theodoulidis, N., 2017. Toward an integrated seismic risk assessment for nuclear safety improving current French methodologies through the SINAPS@ research project. Nucl. Eng. Des. 323, 185–201. https://doi.org/10.1016/j.nucengdes.2016.07.004.

Berge-Thierry, C., Voldoire, F., Ragueneau, F., Lopez-Caballero, F., Le Maoult, A., 2019. Main Achievements of the Multidisciplinary SINAPS@ Research Project: Towards an Integrated Approach to Perform Seismic Safety Analysis of Nuclear Facilities. Pure Appl. Geophys. https://doi.org/10.1007/s00024-019-02194-4.

Bettig, B., Bard, P.Y., Scherbaum, F., Riepl, J., Cotton, F., Cornou, C., Hatzfeld, D., 2001. Analysis of dense array noise measurements using the modified spatial auto-correlation method (SPAC): application to the Grenoble area. Boll. Geofis. Teor. Ed Appl. 42, 281–304.

Bodin, P., Smith, K., Horton, S., Hwang, H., 2001. Microtremor observations of deep sediment resonance in metropolitan Memphis, Tennessee. Eng. Geol. 62, 159–168.

https://doi.org/10.1016/S0013-7952(01)00058-8.

Boncori, J.P.M., Papoutsis, I., Pezzo, G., Tolomei, C., Atzori, S., Ganas, A., Karastathis, V., Salvi, S., Kontoes, C., Antonioli, A., 2015. The February 2014 Cephalonia Earthquake (Greece): 3D Deformation Field and Source Modeling from Multiple SAR Techniques. Seismol. Res. Lett. 86, 124–137. https://doi.org/10.1785/0220140126.

Borges, J.F., Silva, H.G., Torres, R.J.G., Caldeira, B., Bezzeghoud, M., Furtado, J.A., Carvalho, J., 2016. Inversion of ambient seismic noise HVSR to evaluate velocity and structural models of the Lower Tagus Basin, Portugal. J. Seismol. 20, 875–887. https://doi.org/10.1007/s10950-016-9564-x.

Bowen, D.Q., 2010. Sea level ~400 000 years ago (MIS 11): analogue for present and future sea-level? Clim. Past 6, 19–29. https://doi.org/10.5194/cp-6-19-2010.

Briole, P., Elias, P., Parcharidis, I., Bignami, C., Benekos, G., Samsonov, S., Kyriakopoulos, C., Stramondo, S., Chamot-Rooke, N., Drakatou, M.L., Drakatos, G., 2015. The seismic sequence of January–February 2014 at Cephalonia Island (Greece): constraints from SAR interferometry and GPS. Geophys. J. Int. 203, 1528–1540. https://doi.org/10.1093/gji/ggv353.

British Petroleum Co. Ltd, 1971. The Geological Results of Petroleum Exploration in Western Greece. The Geology of Greece. Institute for Geology and Subsurface Research, Athens (73p).

Chandra, J., Guéguen, P., Steidl, J.H., Bonilla, L.F., 2015. In Situ Assessment of the G–γ Curve for Characterizing the Nonlinear Response of Soil: Application to the Garner Valley Downhole Array and the Wildlife Liquefaction Array. Bull. Seismol. Soc. Am. 105, 993–1010. https://doi.org/10.1785/0120140209.

Cheng, H., Lawrence Edwards, R., Shen, C.-C., Polyak, V.J., Asmerom, Y., Woodhead, J., Hellstrom, J., Wang, Y., Kong, X., Spötl, C., Wang, X., Calvin Alexander, E., 2013. Improvements in 230Th dating, 230Th and 234U half-life values, and U–Th isotopic measurements by multi-collector inductively coupled plasma mass spectrometry. Earth and Planetary Science Letters 371–372, 82–91. https://doi.org/10.1016/j.epsl.2013.04.006.

Clément, C., Hirn, A., Charvis, P., Sachpazi, M., Marnelis, F., 2000. Seismic structure and the active Hellenic subduction in the Ionian islands. Tectonophysics 329, 141–156. https://doi.org/10.1016/S0040-1951(00)00193-1.

Cushing, E.M., 1985. Structural evolution of the North-Western Hellenic margin in Levkas Island and Surroundings (North-Western Greece). Zenodo. https://doi.org/10.5281/zenodo.265182.

DISS Working Group, 2015. Database of Individual Seismogenic sources (DISS), Version 3.2.0: A compilation of potential sources for earthquakes larger than M 5.5 in Italy and surrounding areas. https://doi.org/10.6092/INGV.IT-DISS3.2.0.

Douze, E.J., Laster, S.J., 1979. Statistics of semblance. Geophysics 44, 1999–2003. https://doi.org/10.1190/1.1440953.

Eker, A.M., Koçkar, M.K., Akgün, H., 2015. Evaluation of site effect within the tectonic basin in the northern side of Ankara. Eng. Geol. 192, 76–91. https://doi.org/10.1016/j.enggeo.2015.03.015.

EUROCODE8, 1998. Design of structures for earthquake resistance—Part 1: general rules, seismic actions and rules for buildings. European Committee for Standardization, Brussels.

Foti, S., Hollender, F., Garofalo, F., Albarello, D., Asten, M., Bard, P.-Y., Comina, C., Cornou, C., Cox, B., Di Giulio, G., Forbriger, T., Hayashi, K., Lunedei, E., Martin, A., Mercerat, D., Ohrnberger, M., Poggi, V., Renalier, F., Sicilia, D., Socco, V., 2018. Guidelines for the good practice of surface wave analysis: a product of the InterPACIFIC project. Bull. Earthq. Eng. 16, 2367–2420. https://doi.org/10.1007/s10518-017-0206-7.

Ganas, A., Cannavo, F., Chousianitis, K., Kassaras, I., Drakatos, G., 2015. Displacements recorded on continuous GPS stations following the 2014 M6 Cephalonia (Greece) earthquakes: dynamic characteristics and kinematic implications. Acta Geodyn. Geomater. 12 (1), 177. https://doi.org/10.13168/AGG.2015.0005.

Garofalo, F., Foti, S., Hollender, F., Bard, P.Y., Cornou, C., Cox, B.R., Dechamp, A., Ohrnberger, M., Perron, V., Sicilia, D., Teague, D., Vergniault, C., 2016. InterPACIFIC project: comparison of invasive and non-invasive methods for seismic site characterization. Part II: inter-comparison between surface-wave and borehole methods. Soil Dyn. Earthq. Eng. 82, 241–254. https://doi.org/10.1016/j.soildyn.2015.12.009.

Gosar, A., 2007. Microtremor HVSR study for assessing site effects in the Bovec basin (NW Slovenia) related to 1998 Mw5.6 and 2004 Mw5.2 earthquakes. Eng. Geol. 91, 178–193. https://doi.org/10.1016/j.enggeo.2007.01.008.

Gouveia, F., Lopes, I., Gomes, R.C., 2016. Deeper VS profile from joint analysis of Rayleigh wave data. Eng. Geol. 202, 85–98. https://doi.org/10.1016/j.enggeo.2016.01.006.

Guéguen, P., 2016. Predicting Nonlinear Site Response using spectral acceleration Vs PGV/Vs30: a Case history using the Volvi-Test Site. Pure Appl. Geophys. 173, 2047–2063. https://doi.org/10.1007/s00024-015-1224-5.

Guo, Z., Aydin, A., 2016. A modified HVSR method to evaluate site effect in Northern Mississippi considering ocean wave climate. Eng. Geol. 200, 104–113. https://doi.org/10.1016/j.enggeo.2015.12.012.

Guo, Z., Aydin, A., Kuszmaul, J.S., 2014. Microtremor recordings in Northern Mississippi. Eng. Geol. 179, 146–157. https://doi.org/10.1016/j.enggeo.2014.07.001.

Hadler, H., 2013. Ancient Greek harbours used as geo-archives for palaeotsunami research. HEX 2014. Hydrological Extreme Events Hist. Prehist. Times 48.

Haslinger, F., Kissling, E., Ansorge, J., Hatzfeld, D., Papadimitriou, E., Karakostas, V., Makropoulos, K., Kahle, H.-G., Peter, Y., 1999. 3D crustal structure from local earthquake tomography around the Gulf of Arta (Ionian region, NW Greece). Tectonophysics 304, 201–218. https://doi.org/10.1016/S0040-1951(98)00298-4.

Hatzfeld, D., Pedotti, G., Hatzidimitriou, P., Panagiotopoulos, D., Scordilis, M., Drakopoulos, I., Makropoulos, K., Delibasis, N., Latousakis, I., Baskoutas, J., Frogneux, M., 1989. The Hellenic subduction beneath the Peloponnesus: first results of a microearthquake study. Earth Planet. Sci. Lett. 93, 283–291. https://doi.org/10.1016/0012-821X(89)90076-9.

Hollender, F., Cornou, C., Dechamp, A., Oghalaei, K., Renalier, F., Maufroy, E., Burnouf, C., Thomassin, S., Wathelet, M., Bard, P.-Y., Boutin, V., Desbordes, C., Douste-Bacqué, I., Foundotos, L., Guyonnet-Benaize, C., Perron, V., Régnier, J., Roullé, A., Langlais, M., Sicilia, D., 2018. Characterization of site conditions (soil class, VS30, velocity profiles) for 33 stations from the French permanent accelerometric network (RAP) using surface-wave methods. Bull. Earthq. Eng. 16, 2337–2365. https://doi.org/10.1007/s10518-017-0135-5.

Hunter, K.L., 2013. Evaluating the geological, geomorphic and geophysical evidence for the re-location of Odysseus' homeland, "Ancient Ithaca". University of Edinburgh. https://www.era.lib.ed.ac.uk/handle/1842/8002.

Imtiaz, A., Perron, V., Hollender, F., Bard, P., Cornou, C., Svay, A., Theodoulidis, N., 2018. Wavefield Characteristics and Spatial Incoherency: a Comparative Study from Argostoli Rock- and Soil-Site Dense Seismic Arrays. Bull. Seismol. Soc. Am. 108, 2839–2853. https://doi.org/10.1785/0120180025.

Institute of Geology and Mineral Exploration (IGME), 1985. Geological map of Kefalonia Island. Scale 1:50000. Institute of Geology and Mineral Exploration (IGME).

Kassaras, I., Papadimitriou, P., Kapetanidis, V., et al., 2017. Geo-Engineering. In: Sesmic Site Characterization at the Western Cephalonia Island in the Aftermath of the 2014 Earthquake Series. 8. International Journal of Geo-Engineering, pp. 7. https://doi.org/10.1186/s40703-017-0045-z.

Köhler, A., Ohrnberger, M., Scherbaum, F., Wathelet, M., Cornou, C., 2007. Assessing the reliability of the modified three-component spatial autocorrelation technique. Geophys. J. Int. 168, 779–796. https://doi.org/10.1111/j.1365-246X.2006.03253.x.

Lagios, E., Papadimitriou, P., Novali, F., Sakkas, V., Fumagalli, A., Vlachou, K., Del Conte, S., 2012. Combined Seismicity Pattern Analysis, DGPS and PSInSAR studies in the broader area of Cephalonia (Greece). Tectonophysics 524–525, 43–58. https://doi.org/10.1016/j.tecto.2011.12.015.

Le Pichon, X., Chamot-Rooke, N., Lallemant, S., Noomen, R., Veis, G., 1995. Geodetic determination of the kinematics of central Greece with respect to Europe: Implications for eastern Mediterranean tectonics. J. Geophys. Res. Solid Earth 100, 12675–12690. https://doi.org/10.1029/95JB00317.

Lekkas, E., 1996. Neotectonic Map of Greece. Cephalonia—Ithaki sheet. Scale 1: 100.000. University of Athens.

Lisiecki, L.E., Raymo, M.E., 2005. A Pliocene-Pleistocene stack of 57 globally distributed benthic δ ^{18} O records: PLIOCENE-PLEISTOCENE BENTHIC STACK. Paleoceanography 20https://doi.org/10.1029/2004PA001071. n/a-n/a.

Lomax, A., Snieder, R., 1995. 1995. Identifying sets of acceptable solutions to non-linear, geophysical inverse problems which have complicated misfit functions. Nonlinear Process. Geophys 2, 222–227. https://doi.org/10.5194/npg-2-222-1995.

Louvari, E., Kiratzi, A., Papazachos, B., 1999. The Cephalonia Transform Fault and its extension to western Lefkada Island (Greece). Tectonophysics 308, 223–236. https://doi.org/10.1016/S0040-1951(99)00078-5.

Manakou, M.V., Raptakis, D.G., Chávez-García, F.J., Apostolidis, P.I., Pitilakis, K.D., 2010. 3D soil structure of the Mygdonian basin for site response analysis. Soil Dyn. Earthq. Eng. 30, 1198–1211. https://doi.org/10.1016/j.soildyn.2010.04.

Martorana, R., Agate, M., Capizzi, P., Cavera, F., D'Alessandro, A., 2018. Seismo-stratigraphic model of "La Bandita" area in the Palermo Plain (Sicily, Italy) through HVSR inversion constrained by stratigraphic data. Ital. J. Geosci. 137, 73–86. https://doi.org/10.3301/IJG.2017.18.

McMechan, G.A., Yedlin, M.J., 1981. Analysis of dispersive waves by wave field transformation. Geophysics 46, 869–874. https://doi.org/10.1190/1.1441225.

Nakamura, Y., 1989. A method for dynamic characteristics estimation of subsurface using microtremor on the ground surface. Railw. Tech. Res. Inst. Q. Rep. 30, 25–30.

Neidell, N.S., Taner, M.T., 1971. Semblance and other coherency measures for multichannel data. Geophysics 36, 482–497. https://doi.org/10.1190/1.1440186.

Nielsen Dit Christensen, C., 2003. Etude des zones de subduction en convergence hyper-oblique : exemples de la ride méditerranéenne et de la marge indo-birmane (thesis). Paris 11. https://www.theses.fr/2003PA112034.

Özalaybey, S., Zor, E., Ergintav, S., Tapırdamaz, M.C., 2011. Investigation of 3-D basin structures in the İzmit Bay area (Turkey) by single-station microtremor and gravimetric methods: 3-D basin structures of the İzmit Bay area. Geophysical Journal International 186, 883–894. https://doi.org/10.1111/j.1365-246X.2011.05085.x.

Pamuk, E., Gönenç, T., Özdağ, Ö., Akgün, M., 2018. 3D Bedrock Structure of Bornova Plain and its surroundings (İzmir/Western Turkey). Pure Appl. Geophys. 175, 325–340. https://doi.org/10.1007/s00024-017-1681-0.

Papathanassiou, G., Ganas, A., Valkaniotis, S., 2016. Recurrent liquefaction-induced failures triggered by 2014 Cephalonia, Greece earthquakes: Spatial distribution and quantitative analysis of liquefaction potential. Eng. Geol. 200, 18–30. https://doi.org/10.1016/j.enggeo.2015.11.011.

Papathanassiou, G., Valkaniotis, S., Ganas, A., 2017. Evaluation of the macroseismic intensities triggered by the January/February 2014 Cephalonia, (Greece) earthquakes based on ESI-07 scale and their comparison to 1867 historical event. Quat. Int., Quaternary Earthquakes: Geology and Palaeoseismology for Seismic Hazard Assessment 451, 234–247. https://doi.org/10.1016/j.quaint.2016.09.039.

Pérouse, E., 2013. Kinematics and active tectonics of Western Greece in the framework of Central and Eastern Mediterranean geodynamics. Paris Sud (XI), Orsay, France. https://hal.archives-ouvertes.fr/tel-00842274/.

Pérouse, E., Sébrier, M., Braucher, R., Chamot-Rooke, N., Bourlès, D., Briole, P., Sorel, D., Dimitrov, D., Arsenikos, S., 2017. Transition from collision to subduction in Western Greece: the Katouna–Stamna active fault system and regional kinematics. Int. J. Earth Sci. 106, 967–989. https://doi.org/10.1007/s00531-016-1345-9.

Perron, V., Hollender, F., Mariscal, A., Theodoulidis, N., Andreou, C., Bard, P., Cornou, C., Cottereau, R., Cushing, E.M., Frau, A., Hok, S., Konidaris, A., Langlaude, P., Laurendeau, A., Savvaidis, A., Svay, A., 2018. Accelerometer, Velocimeter Dense-Array, and Rotation Sensor Datasets from the Sinaps@ Postseismic Survey (Cephalonia 2014–2015 Aftershock Sequence). Seismol. Res. Lett. 89, 678–687.

https://doi.org/10.1785/0220170125.

Podestá, L., Sáez, E., Yáñez, G., Leyton, F., 2019. Geophysical Study and 3-D Modeling of Site Effects in Viña del Mar, Chile. Earthquake Spectra 35, 1329–1349. https://doi.org/10.1193/080717EQS155M.

Pons-Branchu, E., Hillaire-Marcel, C., Deschamps, P., Ghaleb, B., Sinclair, D.J., 2005. Early diagenesis impact on precise U-series dating of deep-sea corals: example of a 100–200-year old Lophelia pertusa sample from the Northeast Atlantic. Geochim. Cosmochim. Acta 69, 4865–4879. https://doi.org/10.1016/j.gca.2005.06.011.

Pons-Branchu, E., Douville, E., Roy-Barman, M., Dumont, E., Branchu, P., Thil, F., Frank, N., Bordier, L., Borst, W., 2014. A geochemical perspective on Parisian urban history based on U–Th dating, laminae counting and yttrium and REE concentrations of recent carbonates in underground aqueducts. Quat. Geochronol. 24, 44–53. https://doi.org/10.1016/j.gca.2005.06.011.

Protopapa, E., Papastamatiou, D.M., Gazetas, G., 1998. The ionianet accelerometer array: early results and analysis. In: Proc. 11th Eur. Conf. Earthq. Eng.

Reilinger, R., McClusky, S., Vernant, P., Lawrence, S., Ergintav, S., Cakmak, R., Ozener, H., Kadirov, F., Guliev, I., Stepanyan, R., Nadariya, M., Hahubia, G., Mahmoud, S., Sakr, K., ArRajehi, A., Paradissis, D., Al-Aydrus, A., Prilepin, M., Guseva, T., Evren, E., Dmitrotsa, A., Filikov, S.V., Gomez, F., Al-Ghazzi, R., Karam, G., 2006. GPS constraints on continental deformation in the Africa-Arabia-Eurasia continental collision zone and implications for the dynamics of plate interactions. In: EASTERN MEDITERRANEAN ACTIVE TECTONICS, https://doi.org/10.1029/2005JB004051. J. Geophys. Res. Solid Earth 111, n/a-n/a.

Rovithis, E., Pitilakis, K., Lachoulis, T., Karani, I., Chorafa, E., Zarogiani, E., 2014. De Bosset monumental stone bridge in Cephalonia: Strengthening measures and seismic response under the earthquakes of 26/01/2014 and 03/02/2014. In: Presented at the 2nd International Conference on Bridges Innovations on Bridges and Soil-Bridge Interaction, 16–18 October, Athens, Greece.

Sachpazi, M., Hirn, A., Clément, C., Haslinger, F., Laigle, M., Kissling, E., Charvis, P., Hello, Y., Lépine, J.-C., Sapin, M., Ansorge, J., 2000. Western Hellenic subduction and Cephalonia Transform: local earthquakes and plate transport and strain. Tectonophysics 319, 301–319. https://doi.org/10.1016/S0040-1951(99)00300-5.

Saltogianni, V., Moschas, F., Stiros, S., 2018. The 2014 Cephalonia Earthquakes: Finite Fault Modeling, Fault Segmentation, Shear and Thrusting at the NW Aegean Arc (Greece). Pure Appl. Geophys. https://doi.org/10.1007/s00024-018-1938-2.

Saroli, M., Albano, M., Modoni, G., Moro, M., Milana, G., Spacagna, R.-L., Falcucci, E., Gori, S., Scarascia Mugnozza, G., 2020. Insights into bedrock paleomorphology and linear dynamic soil properties of the Cassino intermontane basin (Central Italy). Eng. Geol. 264, 105333. https://doi.org/10.1016/j.enggeo.2019.105333.

Sauret, E.S.G., Beaujean, J., Nguyen, F., Wildemeersch, S., Brouyere, S., 2015. Characterization of superficial deposits using electrical resistivity tomography (ERT) and horizontal-to-vertical spectral ratio (HVSR) geophysical methods: a case study. J. Appl. Geophys. 121, 140–148. https://doi.org/10.1016/j.jappgeo.2015.07.012.

Sbaa, S., Hollender, F., Perron, V., et al., 2017. Analysis of rotation sensor data from the SINAPS@ Kefalonia (Greece) post-seismic experiment—link to surface geology and wavefield characteristics. Earth Planets Space 69, 124. https://doi.org/10.1186/s40623-017-0711-6.

Scordilis, E.M., Karakaisis, G.F., Karacostas, B.G., Panagiotopoulos, D.G., Comninakis, P.E., Papazachos, B.C., 1985. Evidence for transform faulting in the Ionian sea: the Cephalonia island earthquake sequence of 1983. Pure Appl. Geophys. PAGEOPH 123, 388–397. https://doi.org/10.1007/BF00880738.

Sepulcre, S., Durand, N., Bard, E., 2009. Mineralogical determination of reef and periplatform carbonates: Calibration and implications for paleoceanography and radiochronology. Glob. Planet. Change 66, 1–9. https://doi.org/10.1016/j.gloplacha.2008.07.008.

Sorel, D., 1976. Etude néotectonique dans l'arc Egéen externe occidental: les îles Ioniennes de Céphalonie et Zanthe et de l'Elide occidentale (Grèce).

Sorel, D., 1989. L'évolution structurale de la Grèce nord-occidentale depuis le miocène, dans le cadre géodynamique de l'arc égéen. Paris 11.

Sorel, D., Bizon, G., Aliaj, S., Hasani, L., 1992. Calage stratigraphique de l'age et de la duree des phases compressives des Hellenides externes (Grece nord-occidentale et Albanie), du Miocene a l'actuel. Bull. Société Géologique Fr. 163, 447–454.

Souriau, A., Chaljub, E., Cornou, C., Margerin, L., Calvet, M., Maury, J., Wathelet, M., Grimaud, F., Ponsolles, C., Pequegnat, C., Langlais, M., Gueguen, P., 2011. Multimethod Characterization of the French-Pyrenean Valley of Bagneres-de-Bigorre for Seismic-Hazard Evaluation: Observations and Models. Bull. Seismol. Soc. Am. 101, 1912–1937. https://doi.org/10.1785/0120100293.

Stiros, S.C., Pirazzoli, P.A., Laborel, J., Laborel-Deguen, F., 1994. The 1953 earthquake in Cephalonia (Western Hellenic Arc): coastal uplift and halotectonic faulting. Geophys. J. Int. 117, 834–849. https://doi.org/10.1111/j.1365-246X.1994.tb02474.x.

Svay, A., Perron, V., Imtiaz, A., Zentner, I., Cottereau, R., Clouteau, D., Hollender, F., Bard, P.-Y., Lopez-Caballero, F., 2017. Spatial Coherency Analysis of Seismic Ground Motions from a Rock Site Dense Array Implemented during the Kefalonia 2014 Aftershock Sequence. https://doi.org/10.1002/eqe.2881.

SESAME team, 2004. Guidelines for the implementation of the H/V spectral ratio technique on ambient vibrations: measurements, processing and interpretation (Deliverable), WP12. In: SESAME European Research Project.

Theodoulidis, N., Hollender, F., Mariscal, A., Moiriat, D., Bard, P.Y., Konidaris, A., Cushing, M., Konstantinidou, K., Roumelioti, Z., 2018a. The ARGONET (Greece) seismic observatory : an accelerometric vertical array and its data. Seismol. Res. Lett. 89, 1555–1565. https://doi.org/10.1785/0220180042.

Theodoulidis, N., Cultrera, G., Cornou, C., Bard, P.-Y., Boxberger, T., DiGiulio, G., Imtiaz, A., Kementzetzidou, D., Makra, K., the Argostoli NERA Team, 2018b. Basin effects on ground motion: the case of a high-resolution experiment in Cephalonia (Greece). Bull. Earthq. Eng. 16, 529–560. https://doi.org/10.1007/s10518-017-0225-4.

Theodoulidis, N., Karakostas, C., Lekidis, V., Makra, K., Margaris, B., Morfidis, K., Papaioannou, C., Rovithis, E., Salonikios, T., Savvaidis, A., 2016. The Cephalonia, Greece, January 26 (M6.1) and February 3, 2014 (M6.0) earthquakes: near-fault ground motion and effects on soil and structures. Bull. Earthq. Eng. 14, 1–38. https://doi.org/10.1007/s10518-015-9807-1.

Touhami, S., Lopez-Caballero, F., Clouteau, D., 2019. A holistic approach of numerical analysis of the geology effects on ground motion prediction: Argostoli site test. Journal of Seimology Submitted for publication.

Underhill, J.R., 1989. Late Cenozoic deformation of the Hellenide foreland. western Greece. Geol. Soc. Am. Bull. 101, 613–634. https://doi.org/10.1130/0016-7606.

Villemant, B., Feuillet, N., 2003. Dating open systems by the 238 U– 234 U– 230 Th method: application to Quaternary reef terraces. Earth Planet. Sci. Lett. 210, 105–118. https://doi.org/10.1016/S0012-821X(03)00100-6.

Wathelet, M., 2008. An improved neighborhood algorithm: Parameter conditions and dynamic scaling. Geophysical Research Letters 35. https://doi.org/10.1029/2008GL033256.